

©Copyright 2013

Aurora Iris Burd

Three-dimensional electrical conductivity of the
Pampean Shallow Subduction Region
of Argentina near 33S and of the
Payunia region of Argentina near 36.5S

Aurora Iris Burd

A dissertation
submitted in partial fulfillment of the
requirements for the degree of

Doctor of Philosophy

University of Washington

2013

Reading Committee:

John R. Booker, Chair

Jimmy C. Larsen

Kenneth C. Creager

Program Authorized to Offer Degree:
UW Earth and Space Sciences Department

University of Washington

Abstract

Three-dimensional electrical conductivity of the
Pampean Shallow Subduction Region
of Argentina near 33S and of the
Payunia region of Argentina near 36.5S

Aurora Iris Burd

Chair of the Supervisory Committee:
Professor John R. Booker
Earth & Space Sciences Department

I present a three-dimensional (3D) interpretation of long period magnetotelluric sites: 117 from 31 – 35 S and 37 from 35 – 38 S in western Argentina. The first field area covers the most horizontal part of the Pampean shallow angle subduction of the Nazca slab and extends south into the more steeply dipping region. The second field area covers the < 2 Ma Payunia Basaltic Province (PBP). Data from each area were used in 3D Non-Linear Conjugate Gradient inversions.

Three electrically conductive plumes occur at different locations in the crust and upper mantle:

- A plume east of the horizontal Nazca slab rises from near the top of the mantle transition zone at 410 km, through the extrapolated location of the Nazca slab, and extends to the probable base of the lithosphere at 100 km depth.
- A westward dipping plume beneath the PBP rises from roughly 130 km depth to within 7 km of the surface, with two “tendrils” approaching the surface beneath the Caldera Payún Matrú & the Volcán Trómen. These regions have volcanism

younger than 0.1 Ma with some volcanism possibly within the last 7000 years. This plume remains above the subducted Nazca slab.

- An eastward dipping plume rises from at least 410 km depth to within 5 km of the surface while remaining above the subducted Nazca slab, with its shallowest portion beneath the southern region of the PBP, which has no volcanism younger than ~ 0.8 Ma.

Model assessment via both forward modeling and additional inversion tested the veracity of these features.

I interpret the plume near the horizontal Nazca slab as an indication of a slab “window” in the Nazca slab – stress within the slab and seismic tomography support the likelihood of a slab window in this location. I propose that the two plumes beneath the Payunia Basaltic Province were previously a single structure, but the resurgence of mantle shear flow following steepening of a middle to late Miocene shallow slab caused the original plume to be pulled north-westward and eventually “decapitated” to form the two present-day plumes. The west-ward dipping plume likely represents the source of much of the recent Payunia Basaltic Province volcanism.

TABLE OF CONTENTS

	Page
List of Figures	iii
List of Tables	x
Chapter 1: Introduction	1
Chapter 2: Electrical conductivity of the Pampean Shallow Subduction Region of Argentina near 33 S: evidence for a slab window	4
2.1 Authors	4
2.2 Publication Information & Note	4
2.3 Abstract	4
2.4 Introduction	5
2.5 Methods	6
2.6 Results	14
2.7 Discussion	20
2.8 Conclusion	32
2.9 Appendix: Nazca Slab Contours Deeper than 100 km from 23 S to 39 S	32
2.10 Acknowledgments	39
Chapter 3: Three-dimensional electrical conductivity in the mantle beneath the Payún Matrú Volcanic Field in the Andean back-arc of Argentina near 36.5 S	40
3.1 Authors	40
3.2 Publication Information & Note	40
3.3 Summary	41
3.4 Geologic Background	42
3.5 Methods	45
3.6 Results	50

3.7 Discussion	62
3.8 Conclusion	72
3.9 Data Availability	78
3.10 Acknowledgments	78
Bibliography	79

LIST OF FIGURES

Figure Number		Page
2.1	MT Site locations on a topographic map of South America, with slab contours from Appendix A. The green diamonds are MT sites, magenta squares are MT sites used in both this paper and <i>Booker et al.</i> [2004], black triangles are geologically young Southern and Central Volcanic Zone volcanoes, and the dashed gray line is the subducted Juan Fernandez Ridge (JFzR).	12
2.2	Plots of normalized phase tensor skew angle, ψ , for most sites, at each period used in the inversion (some of the Eastern-most sites have been cropped from these images). $ \psi < 6^\circ$ is compatible with 2D interpretation (shown in green in this figure), so most sites are clearly significantly 3D. Small boxes labelled 2004 are sites used in <i>Booker et al.</i> [2004].	13
2.3	(a) East-West slices of resistivity for inversion a53. Slice positions are shown on Figure 2.3(b). Black triangles are Southern Volcanic Zone volcanoes, black lines and dashed lines are location of subducted Nazca slab, based on the slab surface discussed in Appendix A. White points are earthquakes. Scale is stretched North-South to improve viewing. The origin (0,0) = 67° W, 33° S. (b) Position of slices in (a) are shown as solid black lines. Green triangles are MT sites, dashed gray line is the subducted Juan Fernandez Ridge (JFzR), gray line is the subducted Mocha Fracture Zone (MFZ). Black triangles are volcanoes. See the Appendix for dicussion of earthquakes and slab contours. 10 Ohm-m contours of the conductive plume are shown at 200, 250 and 350 km depth. Earthquakes are color-coded by depth. (c) 10 Ohm-m isosurface in red with surface representing subducting slab in shades of green: upper image shows the view to the South (including the underside of the subducting slab) while lower image shows the view to the North.	22

2.4	East-West slices of resistivity for inversion a62. Slice positions are shown on Figure 2.3(b). Black triangles are Southern Volcanic Zone volcanoes, black lines and dashed lines are location of subducted Nazca slab, based on the slab surface discussed in the Appendix. White points are earthquakes. Scale is stretched North-South to improve viewing. The origin (0,0) = 67° W, 33° S.	23
2.5	Maps showing $nRMS$ at each site at each period for a53. Site locations are indicated by the colored circles, where the color corresponds to the $nRMS$ at that site. Note that $0.75 < nRMS < 1.25$ are green to indicate sites at which the inversion was able to adequately fit the data. See text for discussion of why the misfit is not as good at the shorter periods.	24
2.6	Map views showing $P = nRMS/nRMS_0$ at each site in the main part of the array at each period with the conductive plume removed (Test 2 as discussed in the text). Green values are considered insignificant change from the original model. Note that the effect of removing the plume is larger at periods of 465.4 s or longer. This affects the 465.4 s data because the overlying crust is so resistive.	25
2.7	Maps of ratios P and $\delta\psi_\sigma$ at 1280 s period at each site for structural hypothesis tests, displaying only sites in the main array near the conductive plume: (2) conductive plume removed; (3) conductive plume removed above 250 km depth; (4) conductive plume removed below 250 km depth; (5) conductive plume replaced with 10000 Ohm-m layer at 250 km depth; and (6) conductive plume replaced with 10000 Ohm-m layer at 350 km depth. In all images, green dots mean that the model change is allowed by the data; red implies that the model change is forbidden by the data. Boxes A and B are discussed in the text.	26

- 2.8 Focal mechanism beachballs for four Global Centroid Moment Tensors [<http://www.globalcmt.org/CMTsearch.html>]. Tensional (red), compressional (green), and nodal (cyan) axes for these events are shown in the inset. JFzR = Juan Fernandez Ridge, MFZ = Mocha Fracture Zone. 10 Ohm-m plume contours are shown at 200, 250, and 350 km depth. *Anderson et al.* [2007] identify a region of contour-parallel tensional axes in purple box labelled “A” and suggest the possibility of a slab gap in the aseismic region within the purple dashed ovoid. Southern Volcanic Zone volcanoes = black triangles. Stippled gray area is the minimum size of slab window necessary to pass the conductive plume. Serration of the east and south edges indicates that the window may actually extend much further in these directions. 33
- 2.9 Left: horizontal slice of compressional seismic velocity perturbation (δV_p) centered at 249 km depth [*Li et al.*, 2008]. The 250 km contour of the estimated top of the Nazca slab and the 10 Ohm-m contours of the conductive plume at 200, 250 and 350 km depth are shown for comparison. The dashed line “D” is the location of slice *D* in Figure 2.3. Right: vertical slice of the *Li et al.* [2008] model centered on slice *D*. The estimated top of the Nazca slab and the 10 and 30 Ohm-m contours of the conductive plume at this slice are shown for comparison. 34
- 2.10 Four possible ways to create an opening in the slab through which the plume could pass: the “hole” caused by the plume itself; the “scissors”-style contour perpendicular tear as suggested by *Cahill and Isacks* [1992] with the south side dipping more steeply than the north side; the “window” opening initiated by contour-parallel normal faulting; and the “wedge”-style ripping in which the slab is pulled laterally apart. Cross-hatching indicates missing slab; dashed lines indicate the slab hinge; dotted lines indicate slab contours; large arrows indicate down-dip direction; small arrows indicate slab motion or relative motion. 35

2.11 (a) Contours of the minimum curvature surface fit to a series of constraints on the Nazca slab surface deeper than 100 km. Contours are dashed where less certain. Circles filled with color indicating depth are earthquakes with magnitudes ≥ 4.0 from the EHB catalog (1960 – 2008). Diamonds are events from the CHARGE catalog (2000 – 2003). Black triangles are geologically recent volcanoes. JFzR = Juan Fernandez Ridge; MFZ = Mocha Fracture Zone. Constraints on the slab surface consist of: (1) light blue contours from *Linkimer Abarca* [2011]; (2) green contours from *Anderson et al.* [2007]; (3) magenta contours south of 37° S estimated by fitting a plane to EHB events as shown in (b) and (c); (4) magenta 500 and 600 km contours north of 30° S estimated by fitting a plane to deep EHB events from 21.7° S to 29° S as shown in (d), (e) and (f); and (5) six magenta transects along which slab depth has been estimated at about 10 km spacing. Deep earthquakes with magnitude ≥ 4.0 color-coded with their depth are plotted in (d). The 500 and 600 km contours of the best-fitting plane are shown. Their cross-section viewed along strike is shown in (e). The cross-section (f) repeats the fit using only events with magnitude ≥ 5.5 . The data used to construct the transects A, B, C, E, X24 and X35 are summarized in 1:1 cross-sections in the box. Crosses are CHARGE events within $\pm 0.1^\circ$ of the transect; circles are EHB events within the same windows; diamonds are intersections with constraint contours filled with contour color; open squares on transect B are Moment Tensor Centroids; the dark blue filled squares at 400 km on A, E and X35 are estimated from the seismic tomographic slices of *Pesicek et al.* [2012]; the open squares on E and X35 are at the intersection of these two transects. The point labeled X35 on transect A is also on X35. The dashed portion of curve A is not used as a constraint. Finally, the termination of the Nazca slab in a “Tear” at about 38° S is from *Pesicek et al.* [2012]. 38

3.1	<p>(a) Topography of South America, with study region in white box, active Andean Southern Volcanic Zone (SVZ) volcanoes as black triangles, Caldera Payún Matrú as a magenta circle, and contours of subducted slab (after <i>Burd et al.</i> [2013]) in black, with uncertain slab locations indicated with dashed black lines. (b) Payunia region, showing MT sites as green diamonds, active Andean Southern Volcanic Zone volcanoes as black triangles, Caldera Payún Matrú as a magenta circle, Volcán Trómen as a cyan triangle, Cerro Payén as a small white triangle, and Cerro Nevádo as a large white triangle. There are three small pink triangles representing geologically young activity: one is the Los Volcanes region and the other two are single monogenetic centers. Distribution of volcanics and faults is based on <i>Ramos and Folguera</i> [2011]. The Mesozoic Neuquén Basin is outlined in brown dash-dot curves [<i>Howell et al.</i>, 2005] and the basement thrust faults bounding the Proterozoic San Rafael Block are in blue dashed curves. The ~ 1.7 Ma basaltic volcanism of the Payunia region (including the Llanquanelo Volcanic Field that includes Cerro Nevádo) is in gray, with the 1.8–1.6 Ma Trómen Volcanic Field shown in darker gray and the 2–0.8 Ma Auca Mahuida Volcanic Field shown in light gray. The PMVF volcanic products younger than 200 ka are shown in tan. The Cortaderas Lineament aligns with the southern extent of the < 2 Ma volcanism, but is considered by <i>Kay et al.</i> [2006] to be the southern limit of a Miocene shallow subduction region. The slab tear deeper than 200 km based on tomography by <i>Pesicek et al.</i> [2012] is a heavy gray dashed line. Thin gray dashed lines A – E represent transects discussed in the Results section of this paper. The transects are rotated 20° clockwise to match the inversion grid, so that “North” within the grid is N20E in geographic coordinates.</p>	43
3.2	<p>Plots of normalized phase tensor skew angle, ψ for observed data for all sites, at each period used in the inversion. $\psi < 6^\circ$ is compatible with 2D interpretation (shown in green in this figure), so most sites are clearly significantly 3D. North arrow is indicated because inversion grid (and all subsequent analyses) is rotated 20° west of N.</p>	51
3.3	<p>$nRMS$ versus roughness for Payunia inversions with different values of τ (the tradeoff parameter). Blue circles indicate the main inversion sequence, red diamonds are inversions using $\tau = 0.1$, which were used for hypothesis testing (discussed in Model Assessment section), and the green triangle is an inversion using $\tau = 0.1$ with a “tear” at 410 km depth (also discussed in Model Assessment section).</p>	53

3.4	Maps showing $nRMS$ at each site at each period for p207. Site locations are indicated by the coloured circles, where the colour corresponds to the $nRMS$ at that site. Note that $0.75 < nRMS < 1.25$ are green to indicate sites at which the inversion was able to adequately fit the data. Note that the fit is spatially white: fit is equally good at all sites with no particular region being especially poorly fit. Fit is also approximately white by period with the exception of the larger $nRMS$ values at the shortest period. See text for discussion of why the misfit is not as good at the shorter periods.	54
3.5	(a) Nominally East-West slices of resistivity for inversion p207. Slice positions are shown on Fig. 3.1(b). Black triangles are Southern Volcanic Zone volcanoes active in the Holocene, magenta circle is location of Caldera Payún Matrú, black lines and dashed black lines are location of subducted Nazca slab, based on the slab surface discussed in <i>Burd et al.</i> [2013]. White points are earthquakes. Scale is stretched North-South to improve viewing. The origin (0,0) = 69.5° W, 36.5° S. X-axis and Y-axis are measured in km from this origin, and Z-axis is depth in km. (b) 35 Ohm-m isosurface of resistivity, showing DEEP to left and SWAP to right (in red), with subducted slab in green – blue. Volcán Trómen is the black triangle and Caldera Payún Matrú is the magenta circle. Isosurface is looking directly south and shows model deeper than 32 km (i.e. is mantle only). (c) shows only SWAP’s 35 Ohm-m isosurface, but has same legend as (b), except image looks directly west and model is not shown shallower than 8 km. (d) Nominally East-West slices of resistivity for inversion p402, which has a “tear” at 410 km depth (discussed in text). Same caption as Fig. 3.6(a).	56
3.6	Map views showing $P = nRMS/nRMS_0$ at each site at each period with the DEEP removed (Test 1(a) as discussed in the text) and SWAP removed (Test 1(b)). Green values are considered insignificant change from the original model. Note that the effect of removing either plume is larger at longer periods.	66
3.7	Map views showing $\delta\psi_\sigma$ at each site at 1280 s with the DEEP removed (Test 1(a) as discussed in the text) and SWAP removed (Test 1(b)). Green values are considered insignificant change from the original model.	67
3.8	A plot of objective function versus number of iterations for p301 and p302 shows that each inversion’s objective function has converged.	68

3.9	Map legend same as Fig. 3.6(a), but images are map-view slices of resistivity through models p207, p301, and p302 at different depths. Map-views' "east-west" direction is parallel to slices <i>A – E</i> shown on Fig. 3.1(b), with each horizontal slice taking up roughly the area spanned by the five original east-west slices.	69
3.10	Figure is identical to Fig. 3.1(a), with addition of contours corresponding to 35 Ohm-m isosurface of DEEP and SWAP at 33, 52, 129, and 200 km. Transect <i>G</i> shows position of seismic receiver function work of <i>Gilbert et al.</i> [2006] discussed in connection with Fig. 3.11.	73
3.11	60, 30, and 15 Ohm-m contours for SWAP and DEEP from slice <i>C</i> of Figs. 3.1(b) and 3.6(a), superimposed on a receiver function-derived diagram from <i>Gilbert et al.</i> [2006] that corresponds to transect <i>G</i> on Fig. 3.10.	74
3.12	Topographic transect along slice <i>C</i> of Figs. 3.6(a) and 3.10 shows depth of both Pacific and Atlantic Oceans. Inset shows SWAP, DEEP, and subducted Nazca slab, also from slice <i>C</i> : shallowest portion of DEEP corresponds to marked scarp, while SWAP corresponds to Payún Matrú.	75
3.13	Three cartoons depicting evolution of present-day PBP, SWAP, and DEEP. 60, 30, & 15 Ohm-m contours of SWAP & DEEP in green, red, & magenta; subducted Nazca slab location in solid or dashed blue line; Nazca slab motion vectors in blue; mantle flow vectors in brown; PBP in tan; active SVZ at dark blue triangle. (a) shows situation during the end of the Miocene shallow subduction regime, when DEEP and SWAP were one structure just beginning to be sheared north-westward; (b) slab steepening continues through Pliocene, causing increase in mantle flow which shears SWAP and DEEP to north-west, eventually decapitating DEEP to form SWAP; (c) present-day situation based on slice <i>C</i> of Fig. 3.6 – SWAP, DEEP, Nazca slab are to scale, with South America, SVZ, and PBP at correct locations but with exaggerated height.	76

LIST OF TABLES

Table Number	Page
2.1	Selected inversion results. See text for discussion of each quantity. 21
2.2	Hypothesis test results at 1280 s. A total of 114 sites were used at this period for the P -tests and 111 for the $\delta\psi_\sigma$ -tests: columns other than Global $nRMS$ indicate the number of sites in each category. See text for discussion of each test. Global $nRMS$ represents $nRMS$ at all sites and periods used in the inversion. 21
3.1	Hypothesis test results at 1280 s. A total of 37 sites were used at this period for both the P -tests and the $\delta\psi_\sigma$ -tests: columns other than Global $nRMS$ indicate the number of sites in each category. See text for discussion of each test. Global $nRMS$ represents $nRMS$ at all sites and periods used in the inversion. For comparison, global $nRMS$ for p207 is 1.560. 64

ACKNOWLEDGMENTS

I want to express sincere appreciation to John R. Booker, Jimmy C. Larsen, and Randall L. Mackie for many helpful discussions and comments. I also want to thank my parents, sister, and husband for their many years of loving support.

Chapter 1

INTRODUCTION

This dissertation is formed from two papers, “Electrical conductivity of the Pampean Shallow Subduction Region of Argentina near 33 S: evidence for a slab window” (*Geochemistry, Geophysics, Geosystems*, in press) and “Three-dimensional electrical conductivity in the mantle beneath the Payún Matrú Volcanic Field in the Andean back-arc of Argentina near 36.5 S” (*Geophysical Journal International*, in preparation). The “Pampean Shallow Subduction” paper forms the second chapter of my dissertation, while the “Payún Matrú” paper forms the third chapter.

Each paper uses a very large set of magnetotelluric (MT) data. I developed several techniques to facilitate assessment of data misfit, model dimensionality, and model veracity for these extremely large data sets. These techniques included:

- Creation of “polka dot plots” displaying a given data component for each site at each period used in the inversion. Polka dot plots eased the difficulties associated with displaying irregularly-spaced data at multiple periods.

Polka dot plots of “normalized phase tensor skew angle” ψ indicate data dimensionality (Fig. 2.2).

Polka dot plots of $nRMS$ allowed assessment of data misfit (Fig. 2.5).

- Testing the veracity of a 3D structure through two different techniques: (1) by removing the structure from the model and generating new predicted data (the “forward” test) and (2) by removing the structure from the model and allowing the inversion to iterate to convergence (the “inverse” test) – but with

the removed structure forbidden to return. The results of the forward and inverse tests were assessed using:

Polka dot plots of $nRMS/nRMS_0$, which examine the ability of the model to fit the data when a particular 3D feature is removed from the original model (Fig. 2.6).

Polka dot plots of “absolute change in normalized phase tensor skew angle relative to its estimated error” $|\psi - \psi_0|/\sigma$, which show the change in dimensionality of the model when a particular 3D feature is removed from the original model (Fig. 2.7).

The first paper presents a three-dimensional (3D) interpretation of 117 long period (20 to 4096 s) MT sites between 31 S and 35 S in western Argentina. The MT sites cover the most horizontal part of the Pampean shallow angle subduction of the Nazca Plate and extend south into the more steeply dipping region. Sixty-two 3D inversions using various smoothing parameters and data misfits were done with a Non-Linear Conjugate Gradient (NLCG) algorithm. A dominant feature of the mantle structure east of the horizontal slab is a conductive plume rising from near the top of the mantle transition zone at 410 km to the probable base of the lithosphere at 100 km depth. The subducted slab is known to descend to 190 km just west of the plume, but the Wadati-Benioff zone cannot be traced deeper. If the slab is extrapolated down-dip it slices through the plume at 250 km depth. Removal of portions of the plume or blocking vertical current flow at 250 km depth significantly change the predicted responses. This argues that the plume is not an artifact and that it is continuous. The simplest explanation is that there is a “wedge”-shaped slab window that has torn laterally and opens down to the east with its apex at the plume location. Stress within the slab and seismic tomography support this shape. Its northern edge likely explains why there is no deep seismicity south of 29 S.

The second paper presents a 3D interpretation of 37 long period (20 to 5120 s)

MT sites between 35 S and 38 S beneath the < 2 Ma Payunia Basaltic Province, which covers $\sim 39,500$ km² with primarily basaltic intraplate volcanism. This back-arc igneous province is the result of extension due to trench roll-back following steepening of a flat slab that existed in the middle to late Miocene. These data, which require significantly 3D structure, were used in a 3D non-linear conjugate gradient inversion. I identify two significant electrically conductive structures. One approaches the surface beneath the Caldera Payún Matrú & the Volcán Trómen and dips westward toward the subducted Nazca slab. The second approaches the surface ~ 100 km to the southeast and dips steeply east to 400 km depth while remaining above the subducted Nazca slab. I used a variety of model assessment techniques including both forward modeling and additional inversion to test the veracity of these features. I interpret the first structure as the source of the < 2 Ma intraplate volcanism. My inversion model assessment suggests that the shallow structure does not need to connect to the Nazca slab. This is compatible with the lack of recent arc signature magmatism near Payún Matrú. The two structures are electrically connected only in the shallow crust, which is likely due to the Neuquén sedimentary basin and not a magmatic process. I propose that the two structures may have been more robustly connected in the past, but that the deeper structure was decapitated to form the shallower structure when shallow north-westward mantle flow resumed during steepening of the slab. The ~ 2 Ma basaltic volcanism results from the shallow structure's magma that had ponded below the crust until extension allowed eruption. The westward dipping portion of the shallow structure is interpreted as mantle shear in the renewed mantle corner flow – this explains why the shallow structure can appear connected to the Nazca slab near 130 km depth, yet there is no recent arc-signature magma in this region.

Chapter 2

**ELECTRICAL CONDUCTIVITY OF THE
PAMPEAN SHALLOW SUBDUCTION REGION
OF ARGENTINA NEAR 33 S:
EVIDENCE FOR A SLAB WINDOW****2.1 Authors**

- Aurora I. Burd and John R. Booker, Department of Earth & Space Sciences, University of Washington, Seattle, Washington, USA.
- Randall L. Mackie, Land General Geophysics, CGG, Milan, Italy.
- M. Cristina Pomposiello and Alicia Favetto, Instituto de Geocronología y Geología Isotópica, Universidad de Buenos Aires, CONICET, Buenos Aires, Argentina.

2.2 Publication Information & Note

The text in this chapter has been accepted to *Geochemistry, Geophysics, Geosystems* pending minor revisions. The manuscript number is 2013GC004732.

The Appendix of this paper is included in this chapter because it is an integral part of the paper, however it is primarily the work of John R. Booker.

2.3 Abstract

We present a three-dimensional (3D) interpretation of 117 long period (20 to 4096 s) magnetotelluric (MT) sites between 31° S and 35° S in western Argentina. They cover the most horizontal part of the Pampean shallow angle subduction of the Nazca

Plate and extend south into the more steeply dipping region. Sixty-two 3D inversions using various smoothing parameters and data misfits were done with a Non-Linear Conjugate Gradient (NLCG) algorithm. A dominant feature of the mantle structure east of the horizontal slab is a conductive plume rising from near the top of the mantle transition zone at 410 km to the probable base of the lithosphere at 100 km depth. The subducted slab is known to descend to 190 km just west of the plume, but the Wadati-Benioff zone cannot be traced deeper. If the slab is extrapolated down-dip it slices through the plume at 250 km depth. Removal of portions of the plume or blocking vertical current flow at 250 km depth significantly change the predicted responses. This argues that the plume is not an artifact and that it is continuous. The simplest explanation is that there is a “wedge”-shaped slab window that has torn laterally and opens down to the east with its apex at the plume location. Stress within the slab and seismic tomography support this shape. Its northern edge likely explains why there is no deep seismicity south of 29° S.

2.4 Introduction

The subducted Nazca slab beneath Chile and western Argentina, near 31.5° S, levels out at about 100 km depth and then dips more steeply into the mantle several hundred km to the east [Anderson *et al.*, 2007; Cahill and Isacks, 1992; Linkimer Abarca, 2011]. While deep earthquakes north of 29° S locate the slab to a depth exceeding 600 km, the Pampean shallow subduction region does not appear to have any Wadati-Benioff zone earthquakes deeper than 195 km [International Seismological Centre, *EHB Bulletin*, 2010]. The flat slab prevents formation of an asthenospheric wedge under the Andes and consequently there are no active volcanoes. South of 33.3° S in the Andean Southern Volcanic Zone (SVZ), the slab steepens to 36° [Pesicek *et al.*, 2012], an asthenospheric wedge forms and there are active volcanoes. The prevailing view is that the Nazca slab is warped continuously between its flat and dipping segments. For a concise review of Pampean Shallow Subduction, see Ramos [2009].

The resistive crust of the Pampean region permits long period magnetotelluric data to image conductivity at depths of 300 km or more [Booker *et al.*, 2004], and suggests the slab dips steeply at the same longitude as the deep earthquakes north of 29° S. However, the robust result of Booker *et al.* [2004] is that there is vertical current flow at this location and hence a vertical conductor. Identification of this conductor with the slab location rests on its coincidence with southward extrapolation of the very deep earthquakes and the suggestion that the vertical current path is a consequence of penetration of the slab into the transition zone. Thus the location (or even the existence) of the flat Nazca slab after it descends below 200 km is uncertain.

2.5 Methods

The magnetotelluric (MT) method uses passively recorded electric and magnetic field data at Earth’s surface to probe electrical conductivity below Earth’s surface. Electrical conductivity (with units of Siemens per meter) is strongly sensitive to changes in phase (which depends on temperature and pressure), water content, and melt fraction, but between roughly 100 and 400 km depth, elevated conductivity of upper mantle minerals are more likely the result of partial melt or other interconnected fluids than hydrous minerals [Yoshino *et al.*, 2009]. Because conductivity at upper mantle conditions is $\ll 1$, it is usual to use its reciprocal, resistivity (with units of Ohm-m).

From 2000 to 2009, we collected more than 200 MT sites across Argentina, of which 117 between latitudes 29° S and 35° S were used for this study (see Figure 2.1). Analysis of 36 additional sites south of 35° S is in Burd (manuscript in preparation, 2013). Each site consists of 5 to 15 days of horizontal electric field (\mathbf{E} , in units of mV/km) and 3-component magnetic field (\mathbf{H} , in units of nT) time-series sampled at 0.25 s with Narod Intelligent Magnetotelluric Systems (NIMS) or at 5 s with Long-period Intelligent Magnetotelluric Systems (LIMS). The electric field dipoles used Pb-PbCl₂ electrodes [Petiau, 2000].

Time-series data were processed using the robust multi-station algorithm of *Egbert* [1997] to determine the MT impedance tensor \mathbf{Z} and the vertical to horizontal magnetic field transfer function \mathbf{W} , which is also known as the induction vector. These complex frequency-domain transfer functions between the components of the electric and magnetic fields can be written:

$$\begin{bmatrix} E_x \\ E_y \end{bmatrix} = \begin{bmatrix} Z_{xx} & Z_{xy} \\ Z_{yx} & Z_{yy} \end{bmatrix} \begin{bmatrix} H_x \\ H_y \end{bmatrix} \quad (2.1)$$

$$\begin{bmatrix} H_z \end{bmatrix} = \begin{bmatrix} W_x & W_y \end{bmatrix} \begin{bmatrix} H_x \\ H_y \end{bmatrix} \quad (2.2)$$

Each of the elements of \mathbf{Z} and \mathbf{W} in Equations (2.1) and (2.2) has a real and imaginary part, or equivalently, a phase and magnitude. For the impedance tensor, the phases of the impedance elements are defined as

$$\phi_{ij} = \tan^{-1} \left(\frac{\text{Im}(Z_{ij})}{\text{Re}(Z_{ij})} \right) \quad (2.3)$$

and the magnitudes are commonly converted to apparent resistivities

$$\rho_{a,ij} = 0.2T|Z_{ij}|^2 \quad (2.4)$$

where T is the period in seconds. The units of ρ_a are Ohm-m when the units of Z_{ij} are $(mV/km)/nT$. All data were processed identically so that they are directly comparable. These data are available through the *IRIS Data Management System, Seattle, Washington*.

A major step forward in MT interpretation was the realization that \mathbf{Z} can be distorted by un-resolvable small scale structure. When this distortion is due to electric charge that is in-phase with the larger scale “regional” electric field, it is termed static or Galvanic and is a common problem. When the distortion is frequency independent and the regional structure is two-dimensional (2D) it is possible to extract an

estimate of the undistorted regional impedance using techniques that have come to be called “impedance tensor decomposition” [Bahr, 1988; Groom and Bailey, 1989; Jones, 2012]. However, when the regional structure is not strictly 2D, tensor decomposition becomes an invalid statistical model because it cannot fit noise-free measured data [Caldwell *et al.*, 2004; Booker, 2013].

To avoid this fundamental issue, Caldwell *et al.* [2004] introduced the impedance “phase tensor”

$$\mathbf{\Phi} = (\text{Re}(\mathbf{Z}))^{-1} \text{Im}(\mathbf{Z}) = \begin{bmatrix} \Phi_{xx} & \Phi_{xy} \\ \Phi_{yx} & \Phi_{yy} \end{bmatrix} \quad (2.5)$$

$$= \mathbf{R}^{-1}(\theta) \begin{bmatrix} \Phi_a & 0 \\ 0 & \Phi_b \end{bmatrix} \mathbf{R}(\psi) \mathbf{R}(\theta) \quad (2.6)$$

which is un-affected by static distortion and makes no assumptions about the dimensionality of the regional structure. The parameterization (2.6) is related to the geometry of the “phase tensor ellipse” that results when $\mathbf{\Phi}$ multiplies the unit circle [Caldwell *et al.*, 2004; Booker, 2013]. \mathbf{R} is the unitary matrix that rotates Cartesian coordinates through an angle, θ is the direction of one of the axes of the ellipse, $|\Phi_a|$ and $|\Phi_b|$ are the lengths of the ellipse semi-axes and

$$\psi = \tan^{-1} \left(\frac{\Phi_{xy} - \Phi_{yx}}{\Phi_{xx} + \Phi_{yy}} \right) \quad (2.7)$$

is the “normalized phase tensor skew angle”. ψ is rotationally invariant and can be computed in any coordinate system. (Note that ψ is twice the skew angle β defined by Caldwell *et al.* [2004]).

If the regional structure is 2D, ψ must be zero and the principle phases $\phi_a = \tan^{-1}(\Phi_a)$ and $\phi_b = \tan^{-1}(\Phi_b)$ equal the phases of the off-diagonal elements of \mathbf{Z} in the coordinate system aligned with the ellipse axes (i.e. the strike). In that coordinate system the diagonal elements of the 2D regional \mathbf{Z} are 0. If ψ is not zero, the regional structure must be 3D. If $|\psi| = 6^\circ$, the diagonal elements of regional \mathbf{Z} in ellipse-aligned

coordinates are 10% of the off-diagonal elements [Booker, 2013]. Thus $|\psi| > 6^\circ$ is a good working criterion for concluding that the data must be 3D. $|\psi| < 6^\circ$ can be considered “quasi-2D”, but may still be 3D.

Booker *et al.* [2004] analyzed a subset of eighteen of our sites shown as magenta squares in Figure 2.1. They used a 2D non-linear conjugate gradient (NLCG) minimum structure inversion [Rodi and Mackie, 2001]. However, Figure 2.2 also shows ψ at all periods at our 117 sites. Data that meet the quasi-2D criterion of $|\psi| < 6^\circ$ are colored green. It is quite obvious that the data are significantly 3D at most sites and all periods and that deviation from 2D behavior is quite large along the western half of the profile used by Booker *et al.* [2004].

\mathbf{Z} and \mathbf{W} have six complex elements. Their real and imaginary parts constitute twelve responses, which are sensitive to different aspects of resistivity structure. We directly invert the real and imaginary parts of Z_{xx} , Z_{yy} , W_x and W_y . However, instead of directly inverting the real and imaginary parts of the off-diagonal elements Z_{xy} and Z_{yx} , we use their phases and the natural logs of their magnitudes. All twelve inverted responses are in the coordinate system with $x =$ true north and $y =$ true east.

We invert the data using a 3D NLCG minimum structure algorithm (based on Mackie *et al.* [2001]) which seeks a model that minimizes an objective function,

$$S = \chi^2 + \tau R(m) \quad (2.8)$$

where τ is a trade-off parameter, $R(m)$ is a measure of model “roughness” and

$$\chi^2 = \sum_{i=1}^N \frac{r_i^2}{\sigma_i^2} \quad (2.9)$$

is a measure of data misfit. The r_i^2 are the square of the data residuals (e.g. predicted values – observed values), σ_i^2 are the variances, and N is the number of data. The trade-off parameter τ was adjusted between inversion runs in order to minimize S while keeping χ^2 and $\tau R(m)$ of similar order of magnitude so that neither is overly

important. This results in the model that is smoothest (i.e. has least complicated structure) for a given misfit. More complicated models may fit the data equally well but their additional features are not required.

Our algorithm uses weighted least squares. Data with error estimates σ_i smaller than a threshold called the “error floor” are weighted equally while data with larger error estimates are down-weighted. This weighting scheme is implemented by increasing estimated uncertainties below the error floor up to the floor. Henceforth, σ refers to estimated data error after the error floors have been applied.

Instead of χ^2 it is common to give the “normalized RMS”,

$$nRMS = \sqrt{\frac{\chi^2}{N}} \quad (2.10)$$

as the misfit measure because it would be 1.0 if each datum had a misfit equal to its estimated error.

Roughness $R(m)$ can be defined as the square of the Laplacian of the model, averaged over the model. However, because spatial resolution decreases with depth due to the diffusive physics of MT, we modify this definition so that the structure penalty in all spatial directions increases with depth. Making x , y , and z increase logarithmically rather than linearly with depth, a three-dimensional version of the argument of *Smith and Booker* [1991] shows that

$$R(\mathbf{m}) = \int_{model} \left[f_x \frac{\partial^2 \mathbf{m}}{\partial x^2} + f_y \frac{\partial^2 \mathbf{m}}{\partial y^2} + \frac{\partial^2 \mathbf{m}}{\partial z^2} \right]^2 (z + z_0) dx dy dz \quad (2.11)$$

The small scale z_0 prevents the structure penalty from becoming zero at Earth’s surface. The weighting functions

$$f_x = MAX \left(1.0, \frac{\Delta x_i}{\Delta z_k} \right) \quad (2.12)$$

$$f_y = MAX \left(1.0, \frac{\Delta y_i}{\Delta z_k} \right) \quad (2.13)$$

compensate for variable horizontal block widths near the surface, where Δx_i and Δy_i are horizontal block widths in the model and Δz_k is the thickness of each block. $\Delta x_i/\Delta z_k$ and $\Delta y_i/\Delta z_k$ are the block aspect ratios. The weighting functions also account for the large aspect ratios of near-surface blocks that lead to high horizontal roughness.

All models terminate in a 3 Ohm-m half-space deeper than 660 km. A deep resistivity of this order is widely accepted based on mantle conditions and minerals [Xu *et al.*, 2000]. In some of our inversions, a “tear” is added at 410 km depth, at which the smoothing is not enforced. This discontinuity allows assessment of the degree to which this bottom half-space has been smoothed upwards into the rest of the model, as well as whether the data are sensitive to structure below the depth of the tear.

Furthermore, Xu *et al.* [1998] find the phase change from olivine to ringwoodite and wadsleyite (which occurs at roughly 410 km depth) corresponds to a two order of magnitude decrease in resistivity. Yoshino [2010] also documents a decrease in resistivity of at least an order of magnitude at 410 km. Thus there is a geophysical reason to permit a resistivity jump at 410 km.

The inversions include electrically conductive oceans. The importance of the Pacific Ocean in 2D inversions of our data was shown by Booker *et al.* [2005] and the importance of both Pacific and Atlantic Oceans in 3D is discussed by Burd (manuscript in preparation, 2013). In order to keep the mesh size relatively small while accurately modeling the effect of ocean bathymetry, we used an ocean of constant depth but varying electrical conductance. (Conductance [Siemens] = layer thickness [m] \div electrical resistivity [Ohm-m].) This layer has high resistivity when the water is shallow, and low resistivity when the water is deep. The ocean layers and the discontinuity between land and water are excluded from the $R(m)$ computation.

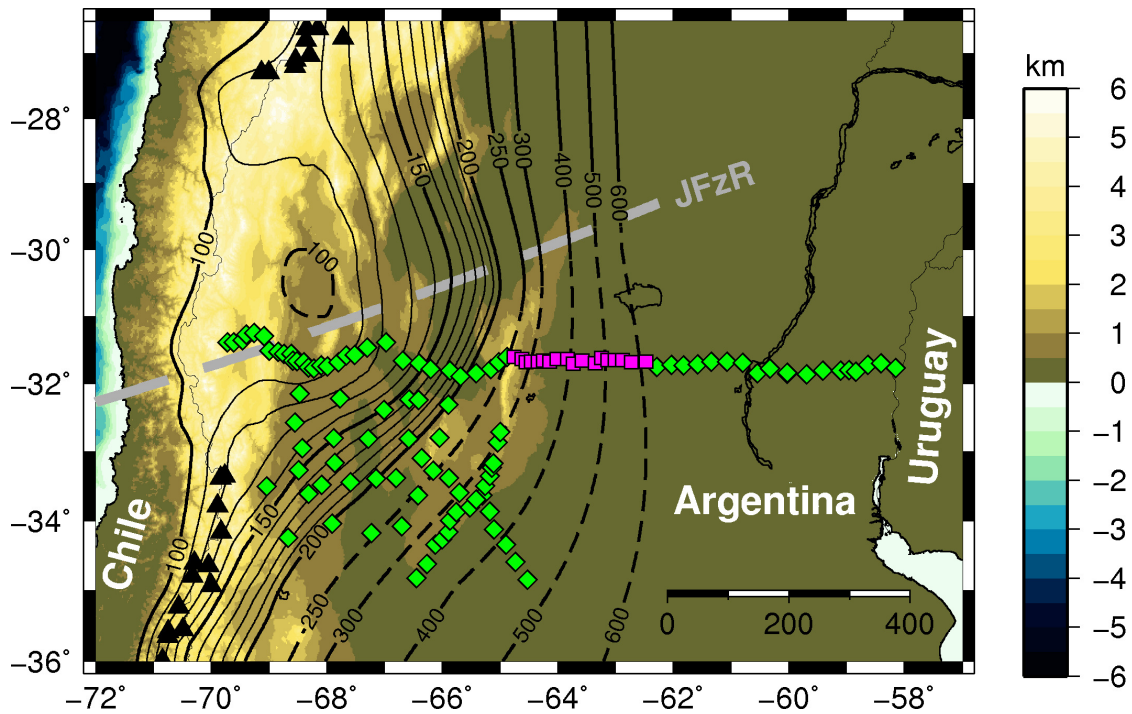


Figure 2.1: MT Site locations on a topographic map of South America, with slab contours from Appendix A. The green diamonds are MT sites, magenta squares are MT sites used in both this paper and *Booker et al.* [2004], black triangles are geologically young Southern and Central Volcanic Zone volcanoes, and the dashed gray line is the subducted Juan Fernandez Ridge (JFzR).

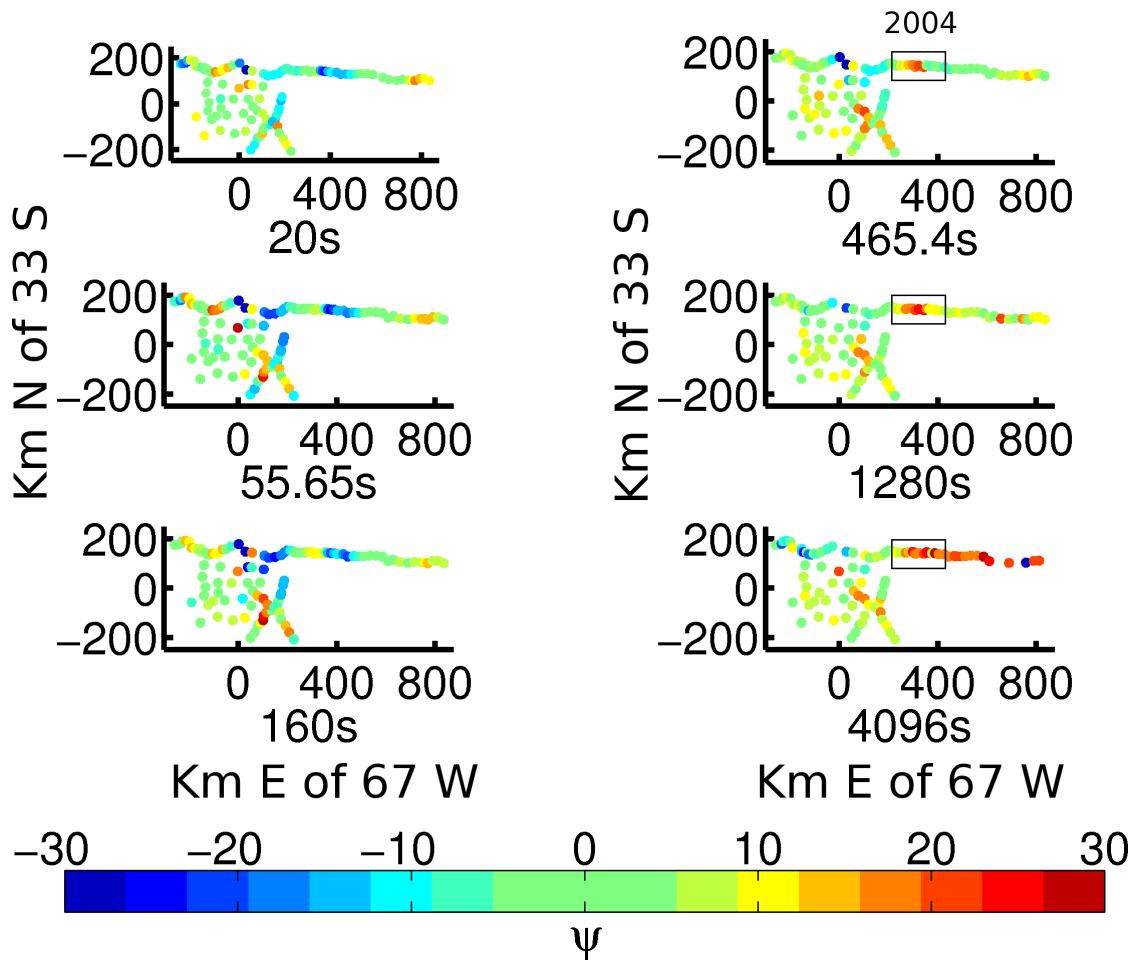


Figure 2.2: Plots of normalized phase tensor skew angle, ψ , for most sites, at each period used in the inversion (some of the Eastern-most sites have been cropped from these images). $|\psi| < 6^\circ$ is compatible with 2D interpretation (shown in green in this figure), so most sites are clearly significantly 3D. Small boxes labelled 2004 are sites used in *Booker et al.* [2004].

2.6 Results

Sixty-two inversions were done using a range of periods, misfit goals, error thresholds, and structure penalty parameters. In order to compare models computed in different ways against each other, forward calculations were made for all models using the same $R(m)$, the same six periods from 20 s to 4096 s, and the same error thresholds: 2% for $|Z_{xy}|$ and $|Z_{yx}|$ (equivalent to 1.2° for ϕ_{xy} and ϕ_{yx} and 4% for the apparent resistivities). The error thresholds for the real and imaginary parts of Z_{xx} are equal to the absolute error threshold of $|Z_{xy}|$, similarly for Z_{yy} and $|Z_{yx}|$.

$nRMS$ and roughness values computed in this way are compared for three inversions in Table 2.1. Each of these inversions was iterated until the objective function (2.8) could no longer be reduced and is considered fully converged. Based on its $nRMS$, “a53” has the best fit to the observed data but is rougher, while “a58” is not as tightly fit and is smoother. Model “a62” has a “tear” at 410 km (as mentioned above in the “Methods” section). Its roughness can not be directly compared to a53 and a58, due to the tear.

Model a53 is considered the best because its $nRMS$ is smallest and all its major features are present in the less tightly fitting and smoother models a58 and a62. While the global $nRMS$ shown in Table 2.1 is useful for comparing different inversions, Figure 2.5 shows the $nRMS$ at each site and period used in a53. Ideally we would like an $nRMS \sim 1.0$ at every site and period, so values of $nRMS$ between 0.75 and 1.25 are shown in green. Since most sites are green at periods longer than 56 s, the global $nRMS$ of 1.91 is largely due to larger misfits at the shortest periods. This is likely the result of trying to fit the responses of shallow structure that have spatial scales smaller than the site spacing and means that the shallow structure is less reliable than deeper structure.

Figure 2.3(a) shows east-west oriented vertical slices through a53. The feature we are concentrating on in this paper is the prominent southwesterly-dipping conductive

plume-like structure between 100 and 410 km depth in the east half of slice *C*. Note that it is deeper and more westerly in slice *B* and shallower and more easterly in slice *D*. The plume’s core is over two orders of magnitude more conductive than the surrounding mantle. This feature is evident in much smoother models that have higher *nRMS* values and is essentially unchanged in models that have tears at 410 km (including a62, which is shown in Figure 2.4).

Appendix A discusses estimation of the subducted slab surface. Figure 2.3(a) shows that the extrapolation of the slab intersects the conductive core of the plume at about 250 km depth. Figure 2.3(b) shows the map view of the slab contours from Figure 2.1 with 10 Ohm-m contours of the model added at 200 km, 250 km, and 350 km depths: the slab and plume intersect at 250 km. Figure 2.3(c) shows the 10 Ohm-m isosurface of the model in red with the subducting slab in shades of green indicating depth, where it is obvious that slab and plume intersect.

It is common at this point in seismological tomographic inversions to use “checker-board” testing to investigate the resolution of the inversions. However, this is not very useful in MT inversions because current must flow continuously from one region to another, so the data collected at a site do not depend only on the local structure. This also implies that the data are sensitive to structure outside of the array.

We thus performed hypothesis tests to answer several questions:

1. Is the inversion’s mid-depth unduly influenced by the bottom boundary condition of a 3 Ohm-m halfspace at 700 km?
2. Is the conductive plume an artifact of the inversion?
3. Is the conductive plume present above the subducted slab’s predicted intersection with the plume location near 250 km depth?
4. Is the conductive plume present below the subducted slab’s predicted intersection with the plume?

5. Is the conductive plume continuous through the predicted intersection with the slab at 250 km?
6. Is the conductive plume continuous through 350 km depth and thus probably connected to the mantle transition below 410 km?

With the exception of interpretation of the effects of the tear in model a62, we used the following procedure to conduct these tests: to determine whether a structure in a particular model is significant, we remove it from the model and see if the responses change by substantially more than the data error. Removing a structure from a converged minimum-structure model is a definitive test of whether the structure is required for the given inversion parameters. In this context we use the data errors after the error floors have been applied because this presents a more challenging test for significance.

For all test results excluding a62's tear, we present two characteristic ratios calculated at each site and period used in the inversion. The first is the ratio of $nRMS$ of the test model to its unperturbed value $nRMS_0$. For brevity, we write

$$P = \frac{nRMS}{nRMS_0} \quad (2.14)$$

The second is the absolute change in normalized phase tensor skew angle relative to its estimated error, which we write:

$$\delta\psi_\sigma = \frac{|\psi - \psi_0|}{\sigma} = \frac{|\Delta\psi|}{\sigma} \quad (2.15)$$

where σ is the estimated error of ψ with error floors applied.

When $P = 1$ there has been no change in $nRMS$, when $P < 1$ the $nRMS$ has decreased (unlikely, but still a possibility), and when $P > 1$ the $nRMS$ has increased. When $P > 2$, it means that the misfit of every datum has on average doubled, which represents very significant worsening of the fit. When $\delta\psi_\sigma < 1$ then $\Delta\psi$ is insignificant

relative to its error, when $1 < \delta\psi_\sigma < 2$ then $\Delta\psi$ is moderately in excess of its error, and when $\delta\psi_\sigma > 2$ then $\Delta\psi$ is at least twice the size of its error. P is useful because it includes both impedance tensor and vertical field data. If all data had the same errors, the error would cancel out of P and P would not depend on the error. In practice, however, data do not all have the same errors, but in our inversion, the error floors make the data errors similar in size and thus P depends only weakly on estimated error and choice of error floor. $\delta\psi_\sigma$ is useful because it is unaffected by shallow distortion, combines all elements of the impedance tensor and is sensitive to changes in structural dimensionality.

Values of both ratios less than one are plotted in green because these values mean that the structural change is allowed by the data. Then we cannot assign geological importance to the structure being tested. On the other hand, $P > 1$ at many sites or $P > 2$ at a few sites can be considered large enough that the change in structure strongly affects the data. In that case, we can be confident that the original structure is not an artifact. Since $\delta\psi_\sigma$ is primarily related to the change in dimensionality of the model and Tests 2 – 6 only change structure near the plume, we expect $\delta\psi_\sigma$ to be much more localized than P . Thus $\delta\psi_\sigma > 1$ at several sites or $\delta\psi_\sigma > 2$ at a few sites indicate that the change in dimensionality of the structure is significant.

We removed conductive structures using a “thresholding” scheme, in which all values with resistivity below 100 Ohm-m were replaced by the largest nearby value. This allows the structure to cease to exist, while avoiding creation of new contrasting structure. In a few cases, however, where we wished to suppress all current flow through a particular structure, we replaced a portion of the conductive structure with very high resistivity (10000 Ohm-m) instead of the more “neutral” structure created using the thresholding scheme. We never use a resistive layer across the entire model because to do so would suppress all vertical current flow, which in particular would significantly alter the effects of the oceans. In general, these structural changes make the test models less 3D. Table 2.2 compiles the results of Tests 2 – 6 at 1280 s, including

the global $nRMS$ found after each test and the number of sites where $1 < P < 2$, $P > 2$, $1 < \delta\psi_\sigma < 2$, and $\delta\psi_\sigma > 2$. 1280 s exhibits the strongest effects. We also present global $nRMS$ using all sites and periods for each test, but we do not compute a global P , since sites far from the test structure and periods insensitive to the test structure will typically cause P to always be close to 1.

2.6.1 Test 1: Sensitivity to Structure Below 410 km

Figure 2.4 shows the results of inversion a62, which has a “tear” at 410 km depth. If the data were not sensitive to structure below the depth of the tear, the region below the tear would have resistivity values identical to the bottom boundary condition of 3 Ohm-m because that is the smoothest possible structure below the tear. Structure below 410 km is visible in all slices, so the data are sensitive to structure below the depth of the tear. In addition, structure above the depth of the tear appears very similar to structure in a53. We conclude that upwards smoothing of the fixed bottom boundary has little effect on the model above 410 km.

2.6.2 Test 2: Existence of Overall Plume

Figure 2.6 shows P at all periods when the conductive plume is removed, and Figure 2.7 (Test 2) shows P and $\delta\psi_\sigma$ at 1280 s. Responses longer than 400 s have $P > 2$ at many sites, indicating that the conductive plume is not an artifact of the inversion. Sites with $\delta\psi_\sigma > 1$ are primarily located in two regions: box A in Figure 2.7 (Test 2) along the main east-west profile and box B, slightly to the south-west. These regions correspond to the location of the plume. Table 2.2 shows that all four P and $\delta\psi_\sigma$ criteria for the structure not being an artifact are met. This test confirms the presence of the conductive feature but does not determine whether it is a single feature or multiple features smeared together.

2.6.3 Test 3: Existence of Plume Above Expected Slab Location

Figure 2.7 (Test 3) shows P and $\delta\psi_\sigma$ for 1280 s when the upper portion of the plume is removed. Compared to removing the entire plume in Test 2, the visual impression of the P map is not quite as strong but there are still many sites with $P > 2$. Sites where $\delta\psi_\sigma > 1$ are mainly located in box A. This is exactly what we expect because this box is above the shallow part of the plume. Table 2.2 shows that all four P and $\delta\psi_\sigma$ criteria are met, indicating that the portion of the plume above 250 km depth is indeed required by the data.

2.6.4 Test 4: Existence of Plume Below Slab Location

Figure 2.7 (Test 4) shows P and $\delta\psi_\sigma$ when the lower portion of the plume is removed. The visual impression of the P map is more subdued than Test 3 but the perturbation in P are still clearly significant. The only sites with $\delta\psi_\sigma > 1$ are in box B which Figure 2.3(b) shows is above the part of the slab deeper than 250 km, as expected. Table 2.2 shows that three of the four P and $\delta\psi_\sigma$ criteria are met, so we conclude that the portion of the plume below 250 km depth is also required by the data.

2.6.5 Test 5: Continuity of Plume Through Predicted Slab Intersection

To test whether electric current flows vertically through the extrapolated slab location, we introduce a horizontal highly resistive 500x500 km thin layer extending across the plume region at 250 km depth. This suppresses all vertical current flow through 250 km at the plume location, and is similar to a test used by *Booker et al.* [2004] to conclude that 2D vertical flow of current from below 200 km is required.

Figure 2.7 (Test 5) shows the P and $\delta\psi_\sigma$ at 1280 s. The P test results are similar in magnitude to Test 4, although somewhat differently arrayed spatially. Like Test 4, the only sites with $\delta\psi_\sigma > 1$ are in box B but show a larger effect. Table 2.2 shows that all four of the P and $\delta\psi_\sigma$ criteria are met. We therefore conclude that vertical current

flow is required by the data, and that there is a single plume extending through the estimated slab location at 250 km depth.

2.6.6 Test 6: Vertical Current Flow Between Plume and Transition Zone

Figure 2.3(a) shows the plume emerging from the top of a widespread deep conductor that extends across the entire model, which can reasonably be identified with a conductive mantle transition zone that begins at 410 km, but the deepest layer at which the plume is readily identifiable as a conductive zone in a resistive environment is slightly shallower, at 350 km. Thus we introduce a horizontal highly resistive 500×750 km layer at 350 km to block vertical current flow between the plume and the transition zone.

Figure 2.7 (Test 6) shows that no sites have $P > 2$ or $\delta\psi_\sigma > 1$ at 1280 s, however 40 sites spread over much of the main array have $P > 1$. Table 2.2 shows that only one of the P criteria and none of the $\delta\psi_\sigma$ criteria are met. Tables 2.1 and 2.2 also show that the global $nRMS$ of this test is nearly the same as the global $nRMS$ of a53, which suggests that most values of P are actually near 1. Based on our criteria, we can not conclude that vertical current flow through 350 km is required by the data. However, Test 6 may be inadequate because the model at this depth is in general more conductive, so it is harder to block the three-dimensional flow of current with a resistive layer local to the plume. Therefore current may easily flow around the resistive layer, causing P and $\delta\psi_\sigma$ to be near one at most sites, yielding a misleading conclusion.

2.7 Discussion

Our tests show that the conductive plume is required by the data, and the data require the plume to be a continuous feature above 350 km which passes through the estimated slab location. Similar tests were performed on model a62, with identical outcomes.

Table 2.1: Selected inversion results. See text for discussion of each quantity.

Inversion Name	a53	a58	a62
<i>Global nRMS</i>	1.91	2.08	2.32
<i>Roughness</i>	$5.7x10^6$	$4.0x10^6$	$1.3x10^6$
<i>Number of iterations</i>	252	152	170

Table 2.2: Hypothesis test results at 1280 s. A total of 114 sites were used at this period for the P -tests and 111 for the $\delta\psi_\sigma$ -tests: columns other than *Global nRMS* indicate the number of sites in each category. See text for discussion of each test. *Global nRMS* represents *nRMS* at all sites and periods used in the inversion.

Test	<i>Global nRMS</i>	$1 < P < 2$	$P > 2$	$1 < \delta\psi_\sigma < 2$	$\delta\psi_\sigma > 2$
<i>Test 2</i>	2.39	66	40	13	4
<i>Test 3</i>	2.52	60	40	12	2
<i>Test 4</i>	2.06	71	8	6	0
<i>Test 5</i>	1.99	72	2	7	2
<i>Test 6</i>	1.92	43	0	0	0

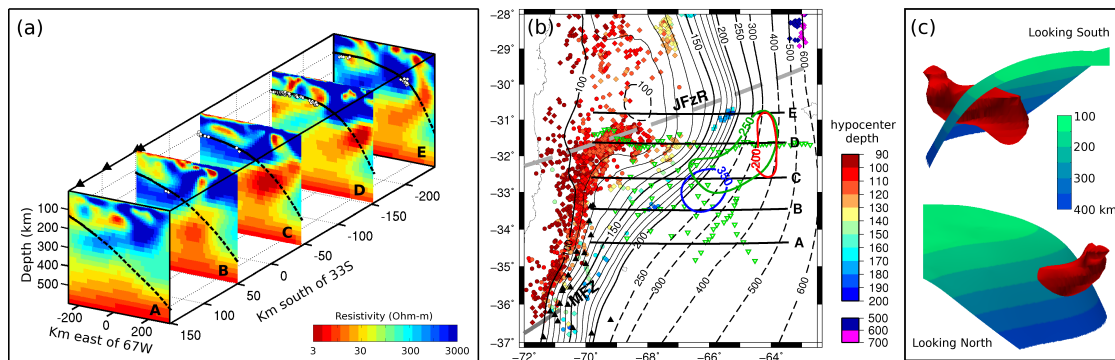


Figure 2.3: (a) East-West slices of resistivity for inversion a53. Slice positions are shown on Figure 2.3(b). Black triangles are Southern Volcanic Zone volcanoes, black lines and dashed lines are location of subducted Nazca slab, based on the slab surface discussed in Appendix A. White points are earthquakes. Scale is stretched North-South to improve viewing. The origin (0,0) = 67° W, 33° S. (b) Position of slices in (a) are shown as solid black lines. Green triangles are MT sites, dashed gray line is the subducted Juan Fernandez Ridge (JFzR), gray line is the subducted Mocha Fracture Zone (MFZ). Black triangles are volcanoes. See the Appendix for discussion of earthquakes and slab contours. 10 Ohm-m contours of the conductive plume are shown at 200, 250 and 350 km depth. Earthquakes are color-coded by depth. (c) 10 Ohm-m isosurface in red with surface representing subducting slab in shades of green: upper image shows the view to the South (including the underside of the subducting slab) while lower image shows the view to the North.

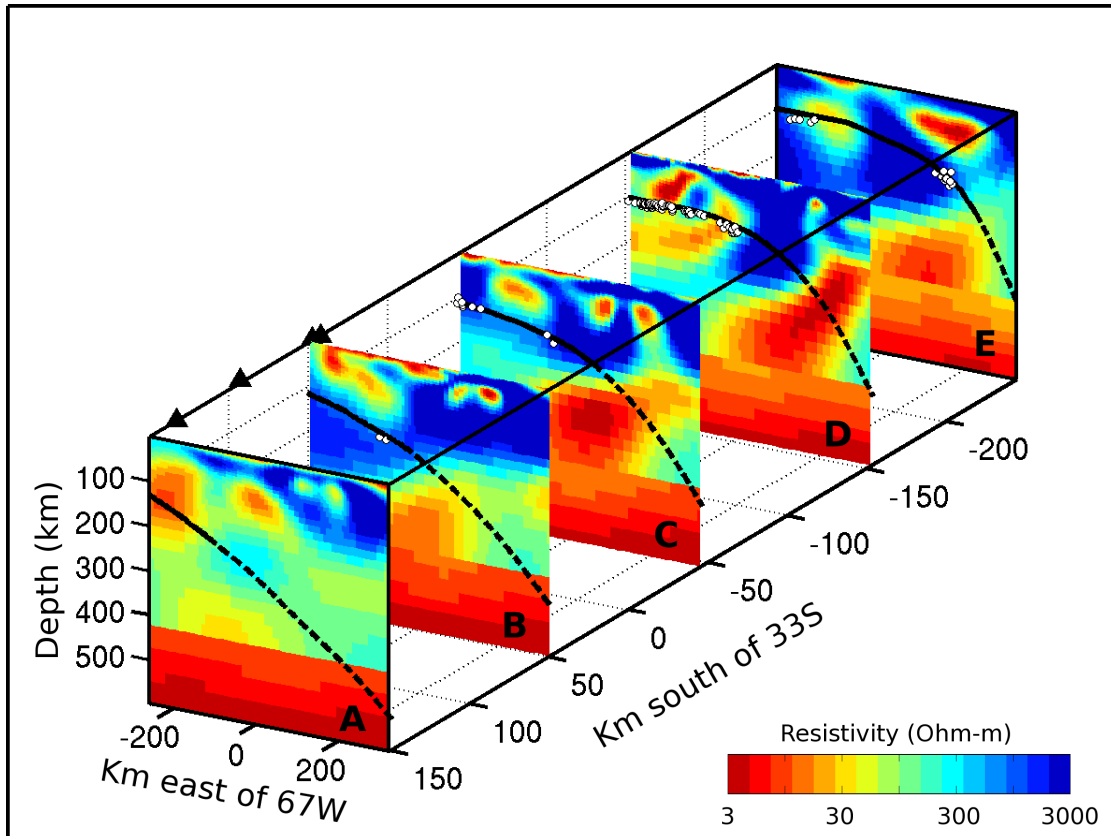


Figure 2.4: East-West slices of resistivity for inversion a62. Slice positions are shown on Figure 2.3(b). Black triangles are Southern Volcanic Zone volcanoes, black lines and dashed lines are location of subducted Nazca slab, based on the slab surface discussed in the Appendix. White points are earthquakes. Scale is stretched North-South to improve viewing. The origin (0,0) = 67° W, 33° S.

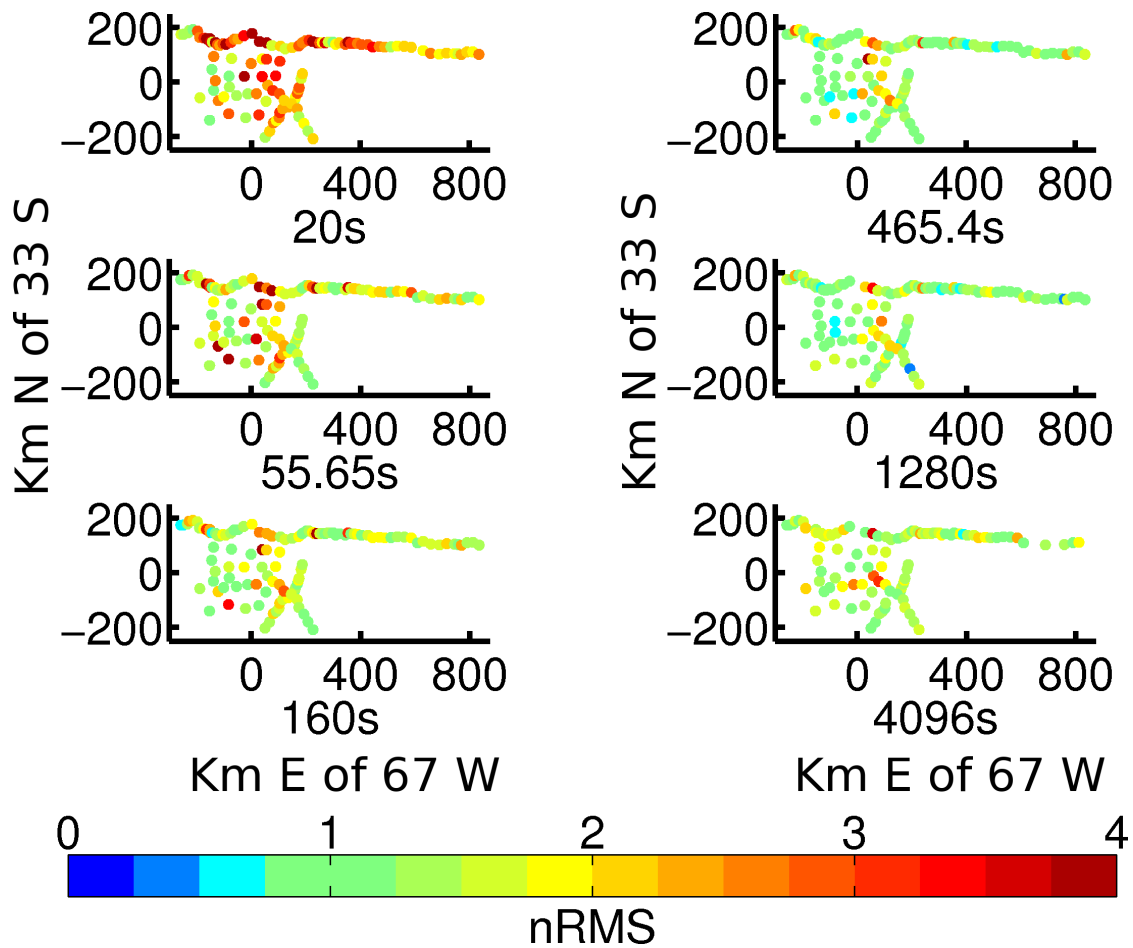


Figure 2.5: Maps showing $nRMS$ at each site at each period for a53. Site locations are indicated by the colored circles, where the color corresponds to the $nRMS$ at that site. Note that $0.75 < nRMS < 1.25$ are green to indicate sites at which the inversion was able to adequately fit the data. See text for discussion of why the misfit is not as good at the shorter periods.

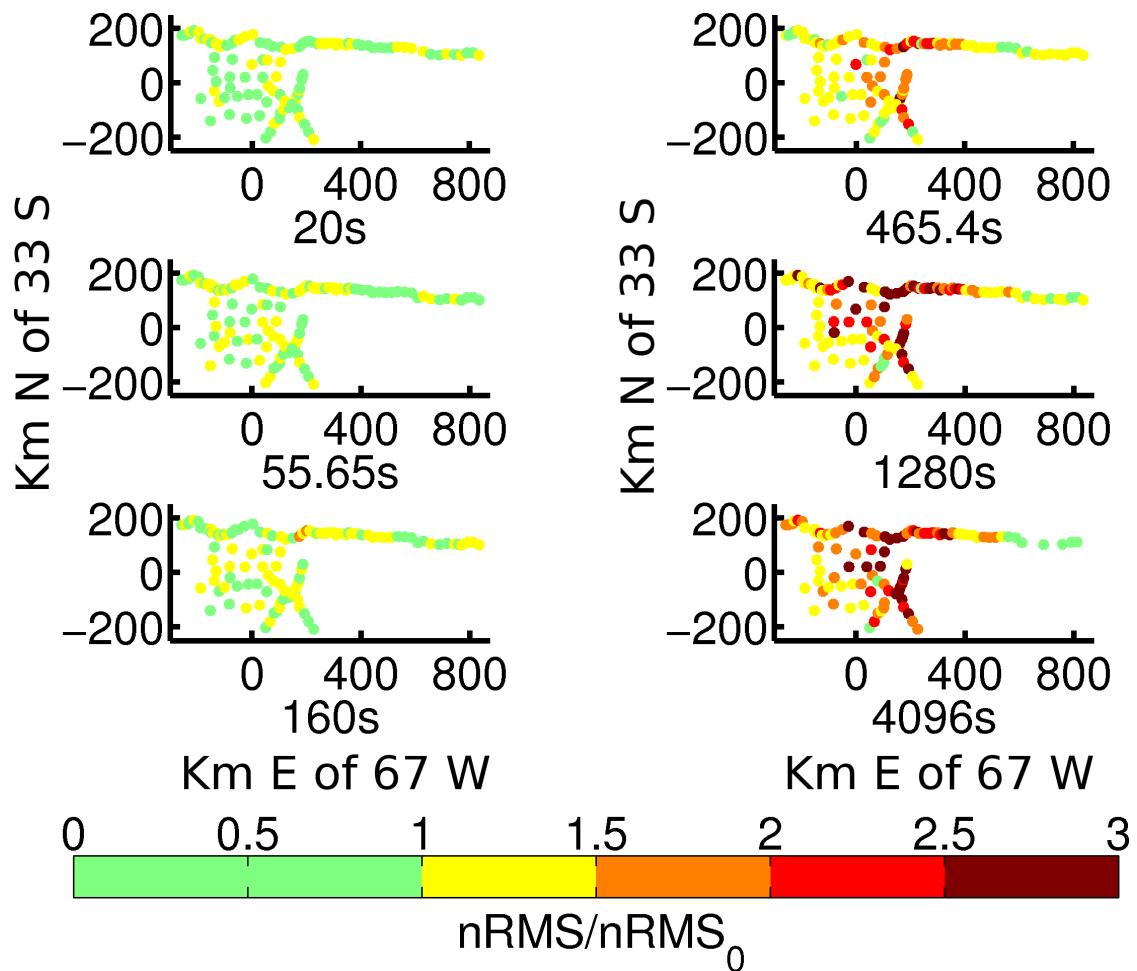


Figure 2.6: Map views showing $P = nRMS/nRMS_0$ at each site in the main part of the array at each period with the conductive plume removed (Test 2 as discussed in the text). Green values are considered insignificant change from the original model. Note that the effect of removing the plume is larger at periods of 465.4 s or longer. This affects the 465.4 s data because the overlying crust is so resistive.

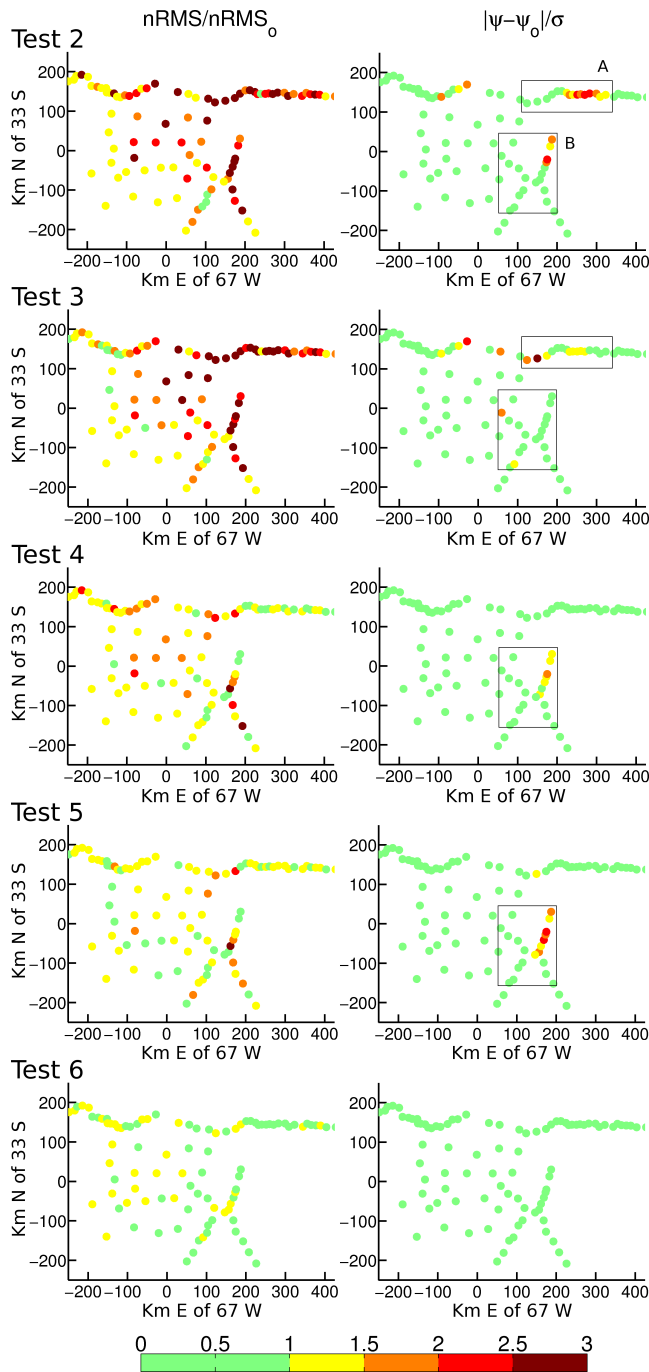


Figure 2.7: Maps of ratios P and $\delta\psi_\sigma$ at 1280 s period at each site for structural hypothesis tests, displaying only sites in the main array near the conductive plume: (2) conductive plume removed; (3) conductive plume removed above 250 km depth; (4) conductive plume removed below 250 km depth; (5) conductive plume replaced with 10000 Ohm-m layer at 250 km depth; and (6) conductive plume replaced with 10000 Ohm-m layer at 350 km depth. In all images, green dots mean that the model change is allowed by the data; red implies that the model change is forbidden by the data. Boxes A and B are discussed in the text.

There are at least three possible scenarios that allow electric current to flow through the estimated slab location: (1) the slab is sufficiently deformed so that the plume is always east of the slab; (2) there is a window in the slab where the plume and slab intersect; and (3) a deep plume impinges on the slab and generates a shallow plume that is electrically but not mechanically connected to the deep plume.

The first possibility seems untenable. Figure 2.3(b) shows that the 10 Ohm-m contour passes under the 170 km slab contour at 31.5° S. This contour is constrained by hypocenters within a degree to the southwest and northwest and within half a degree up-dip. Thus a continuous slab that remains west of the plume would need to fold back on itself and dip steeply westward between 32 and 33° S. However the tomographic model of *Pesicek et al.* [2012] images the slab at 35° S with an average eastward dip of 36° from 200 to 400 km depth while the deep seismicity at 29° S implies an eastward slab dip of about 65° (see Appendix A). Consequently, a reverse dip between 32 and 33° S would require an unlikely amount of distortion.

The second alternative is supported by three lines of evidence: observed stress within the slab, seismic tomography and our electrical conductivity structure. Intermediate depth subduction zone earthquakes are expected to exhibit downdip tension and normal faulting when the subducted slab is mechanically continuous to deeper depths, because the denser, deeper slab pulls on the buoyant, shallower slab. Regional studies of slab stress in the Chile-Argentina subduction zone [*Chen et al.*, 2001; *Slancová et al.*, 2000; *Anderson et al.*, 2007; *Pardo et al.*, 2002] support this concept. However, *Anderson et al.* [2007] find focal mechanism tension (T) axes for events about 120 km deep within the box labelled A in Figure 2.8 to be predominantly along the depth contours (i.e. perpendicular to their expected direction) and they suggest a slab window roughly coincident with the aseismic dashed ovoid to the east-southeast of their box.

Figure 2.8 also shows four focal mechanism beachballs for the best double-couple Centroid Moment Tensors [<http://www.globalcmt.org/CMTsearch.html>] deeper than

150 km and northeast of box A. Their T, P (compression) and nodal axes are shown on a stereo plot in the inset. Although their P and nodal axes directions are diverse, their T axes are closely grouped with a mean direction to the northeast and a dip near 20° . Like the *Anderson et al.* [2007] events, this direction is not perpendicular to the subducting slab's contours, but instead points towards the southern end of the very deep seismicity at 29° S. This suggests that while the slab may be continuous between these four events and the deep events, the subducted slab is missing to the south-east.

Figure 2.9 shows horizontal and vertical slices of the global seismic tomography model of *Li et al.* [2008]. These slices show the percentage change of compressional body wave velocity V_p with respect to the assumed radially symmetric background. The horizontal block dimensions are $0.7^\circ \times 0.7^\circ$ and the vertical thicknesses are 45.2 km. Although one needs to be cautious about local inferences from global seismic tomography, there is a remarkable coincidence between features of this model and our conductive plume. The horizontal slice on the left is centered at 249 km depth. North of 31° S it has high velocity that compares very well with the 250 km estimated slab contour. South of 31° S this slab signature essentially terminates and appears to resume again to the southwest. The 10 Ohm-m contour of the conductive plume at 250 km depth fits neatly into the gap in the slab signature. The vertical slice of δV_p at slice *D* of Figure 2.3 is shown on the right of Figure 2.9. Again there is high velocity that can be associated with the Nazca Slab shallower than 200 km and deeper than 350 km. Between 200 and 350 km the slab signature is missing. The 10 and 30 Ohm-m contours of the conductive plume fit neatly into this gap. These correspondences seem unlikely to be fortuitous and we conclude that the slab is missing where it would intersect the plume. Deeper than 350 km, the high seismic velocity suggests that the slab is present again. However, the slab signature arguably dips westward below this depth and ends up beneath the apparent source of the conductive plume. This suggests that the deeper slab signature may not be the Nazca Slab, but a relic

of earlier, westward dipping subduction.

The gray stippled area in Figure 2.8 shows the approximate minimum extent of the slab window necessary to allow the plume to pass through. The western boundary is the 200 km slab contour, as the slab is relatively well-located to this depth. The northern boundary is parallel to the T axes of the four earthquakes discussed earlier in this section, and its eastward extension passes through the southern termination of the very deep seismicity. It is shown with a dashed line because its exact position is uncertain. The eastern boundary is based on the deep slab δV_p signature seen in Figure 2.9. However, it is possible that the slab window continues downward to the east, as this would explain why there are no very deep earthquakes south of 29° S; this is also compatible with our results, so the eastern boundary is shown as a serrated edge. The southern extent of the slab window is also uncertain (and is shown with a serrated edge), but since *Pesicek et al.* [2012] image a continuous slab at 35° S to 400 km, the slab window must terminate north of 35° S.

It is intriguing to note that extrapolation of the Mocha Fracture Zone (MFZ) coincides with the southern edge of our plume, although *Tebbens and Cande* [1997] and *Folguera and Ramos* [2009] imply that the MFZ does not continue far enough inland to reach our plume. *Tebbens and Cande* [1997] identify a putative piece of the MFZ 500 km west of South America. This western segment of a transform fault appears to end between chron 10 (~ 28 Ma) and chron 13 (~ 33 Ma), which implies that the matching segment of the transform fault on the other side of the spreading center must also end between chron 10 and chron 13. The age of the seafloor currently subducting where the MFZ meets South America is between chron 10 and chron 13. Thus correlation of the two pieces of transform with the western and eastern ends of the MFZ is clearly reasonable and if correct, implies that the MFZ does not extend very far beneath South America. *Folguera and Ramos* [2009] argue that subduction of the eastern end of the MFZ initiated deformation in the Andes at roughly 3.6 Ma and that the MFZ ends beneath the Andes at about (36.5° S, 71° W).

The third alternative of electrically but not mechanically coupled plumes above and below the slab is not easy to dismiss. Above the mantle transition zone from 410 to 660 km (MTZ) but deeper than 250 km it is extremely difficult to reduce upper mantle resistivity below 10 Ohm-m with high temperature and pressure alone [Yoshino *et al.*, 2012]. Thus low resistivity of the plume below the slab almost certainly requires either an interconnected fluid fraction with partial melt being the leading candidate [Yoshino *et al.*, 2009] or a very high concentration of dissolved water (0.1%) [Poe *et al.*, 2010]. If such a plume meets the slab it need not pass through to lower the slab resistivity. Instead it may locally elevate the slab temperature enough to release sufficient water to generate another plume rising above the slab. Such a slab “lesion” would have low seismic velocity and is very unlikely to be able to support tensile stress or generate seismicity and could thus explain the observations just as well as a plume that passes through a window in the slab. Since we cannot yet offer a definitive test of this alternative we have to leave it as an open possibility, but in the absence of other evidence pointing to this possibility, we conclude that a slab window is the most likely explanation for our results.

Our electrically conductive plume is both similar to and different from the main conductive structure found by Booker *et al.* [2004]. Similarities include the fact that both structures are much more conductive than the surrounding mantle, and both structures appear to extend from near the top of the MTZ at 410 km depth but do not penetrate the base of the lithosphere at about 100 km. Booker *et al.* [2004], however, conclude that their conductor is parallel to and east of a steeply-dipping slab. Our 3D plume is very similar to Booker *et al.* [2004] down to 200 km but deviates more than 200 km to the southwest as depth increases and thus cannot remain east of even a very steeply-dipping slab. Nevertheless, the fundamental conclusion of Booker *et al.* [2004] from their 2D study remains: there is a conductive feature extending up from near the 410 km seismic transition. It is encouraging that a 2D interpretation of a clearly 3D structure has such a close resemblance to the 3D interpretation.

We can only speculate about why there is a slab window and an electrically conductive plume at this location. We consider four possibilities. (1) Since the plume conductivity is likely due to the presence of partial melt, it could be a nascent hot spot or asthenospheric plume such as has been suggested in the Cascadia backarc (G. Egbert, Three-dimensional Inversion of EarthScope Magnetotelluric Data: crustal and mantle conductivity beneath the NW USA, IRIS Webinar: <http://www.iris.edu/hq/webinar/>, 2013). (2) *Booker et al.* [2004] suggest that residual slab water at the intersection of the downgoing slab with the MTZ triggers the plume. This argument is no longer viable, as our plume and the projected Nazca slab enter the MTZ in different places. (3) Figure 2.9 suggests a relic slab in the MTZ under the origin of our plume: it is possible that the presence of this relic slab in the MTZ is responsible for the plume. (4) The plume is a consequence of the slab window’s formation. We do not have an explanation for why this should be.

The opening through which the plume passes may be caused by the plume itself or be the result of the geometry of the subduction. In addition to a plume-caused “Hole”, three variations are shown in Figure 2.10. The “Scissors”-style contour-perpendicular tear configuration with vertical offset is suggested by *Cahill and Isacks* [1992]. This geometry requires the deep plume to jog to the south-east through the gap before rising further. It is clear from Figure 2.3(c), however, that the plume jogs to the north-east, which would imply scissoring with the north side down and require the flat slab to be to the south. As this configuration does not exist, this type of tear can be ruled out. The “Window” opening would start with contour-parallel normal faulting, with a piece of slab descending faster. This is essentially a small version of a subducted oceanic ridge. Trench-parallel faults are known to exist in the slab [*Gans et al.*, 2011], which at depth could allow denser, deeper slab to easily tear away. This kind of slab window requires strike-slip faulting. These strike-slip faults could be reactivated features parallel to the slab motion, such as those associated with the Juan Fernandez Ridge or perhaps the Mocha Fracture Zone. However, we favor “Wedge”-

style ripping in which the two pieces of slab are pulled laterally apart. The geometry of the flat slab produces significant lateral membrane stresses [*Creager et al.*, 1995], which would be largely relieved upon opening of such a wedge. The plume should facilitate this process by heating the apex of the wedge. In this case, the wedge should probably extend downward through the entire slab, which would require that the deep slab shown on the right side of Figure 2.9 be a westward dipping relic slab, as discussed earlier. We propose that the termination of the very deep earthquakes at 29° S likely coincides with the northern boundary of the wedge.

2.8 Conclusion

Results of a 3D minimum-structure inversion yield an image of the electrical conductivity beneath the Pampean Shallow Subduction region in western Argentina. We have demonstrated the existence of an electrically conductive plume that passes through the extrapolated slab location at about 250 km. We conclude that a “wedge”-shaped slab window with its apex at the plume location best explains all the evidence.

2.9 Appendix: Nazca Slab Contours Deeper than 100 km from 23 S to 39 S

To see whether the electrically conductive plume intersects the subducted slab it is necessary to predict the slab depth below 200 km. We have constructed a slab that is consistent with available data and is extrapolated with minimum structure away from the constraints. Our goal was to produce a surface deeper than 150 km that is consistent with all available data. The result, valid from 100 to 600 km depth, is shown in Figure 2.9.

This new slab surface is a minimum curvature fit to a series of constraints that are also presented in Figure 2.9. These constraints start with a subset of shallow contours that set the boundary condition on the shallow slab dip. From 33° S to 37° S we use the 140, 150 and 160 km contours of *Anderson et al.* [2007]. These

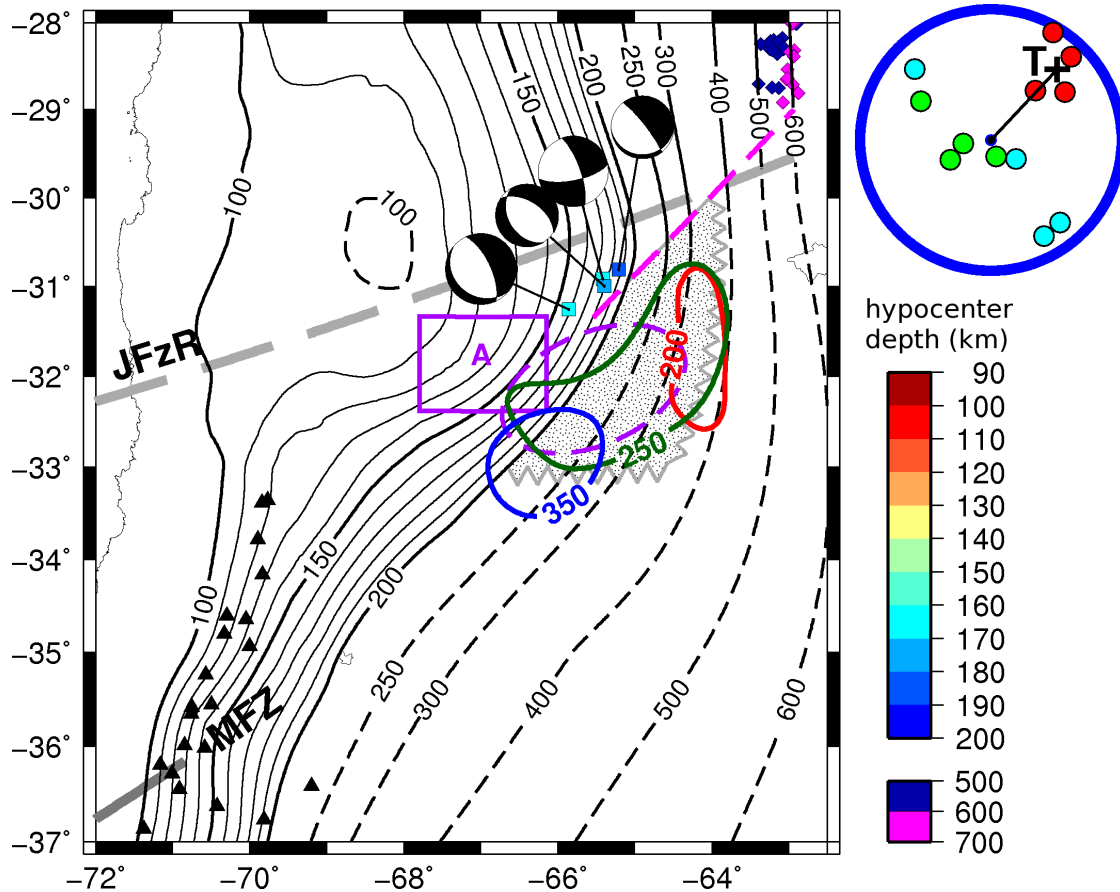


Figure 2.8: Focal mechanism beachballs for four Global Centroid Moment Tensors [<http://www.globalcmt.org/CMTsearch.html>]. Tensional (red), compressional (green), and nodal (cyan) axes for these events are shown in the inset. JFzR = Juan Fernandez Ridge, MFZ = Mocha Fracture Zone. 10 Ohm-m plume contours are shown at 200, 250, and 350 km depth. *Anderson et al.* [2007] identify a region of contour-parallel tensional axes in purple box labelled “A” and suggest the possibility of a slab gap in the aseismic region within the purple dashed ovoid. Southern Volcanic Zone volcanoes = black triangles. Stippled gray area is the minimum size of slab window necessary to pass the conductive plume. Serration of the east and south edges indicates that the window may actually extend much further in these directions.

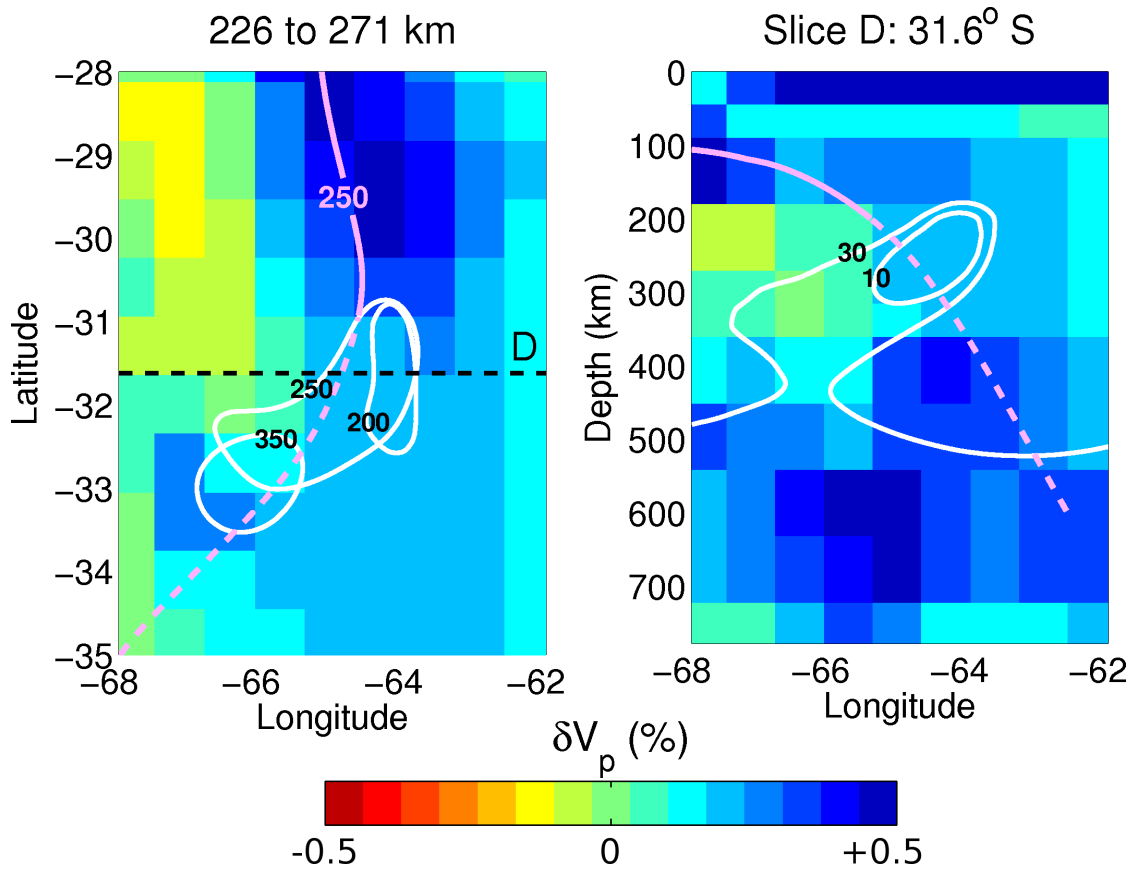


Figure 2.9: Left: horizontal slice of compressional seismic velocity perturbation (δV_p) centered at 249 km depth [Li *et al.*, 2008]. The 250 km contour of the estimated top of the Nazca slab and the 10 Ohm-m contours of the conductive plume at 200, 250 and 350 km depth are shown for comparison. The dashed line “D” is the location of slice *D* in Figure 2.3. Right: vertical slice of the Li *et al.* [2008] model centered on slice *D*. The estimated top of the Nazca slab and the 10 and 30 Ohm-m contours of the conductive plume at this slice are shown for comparison.

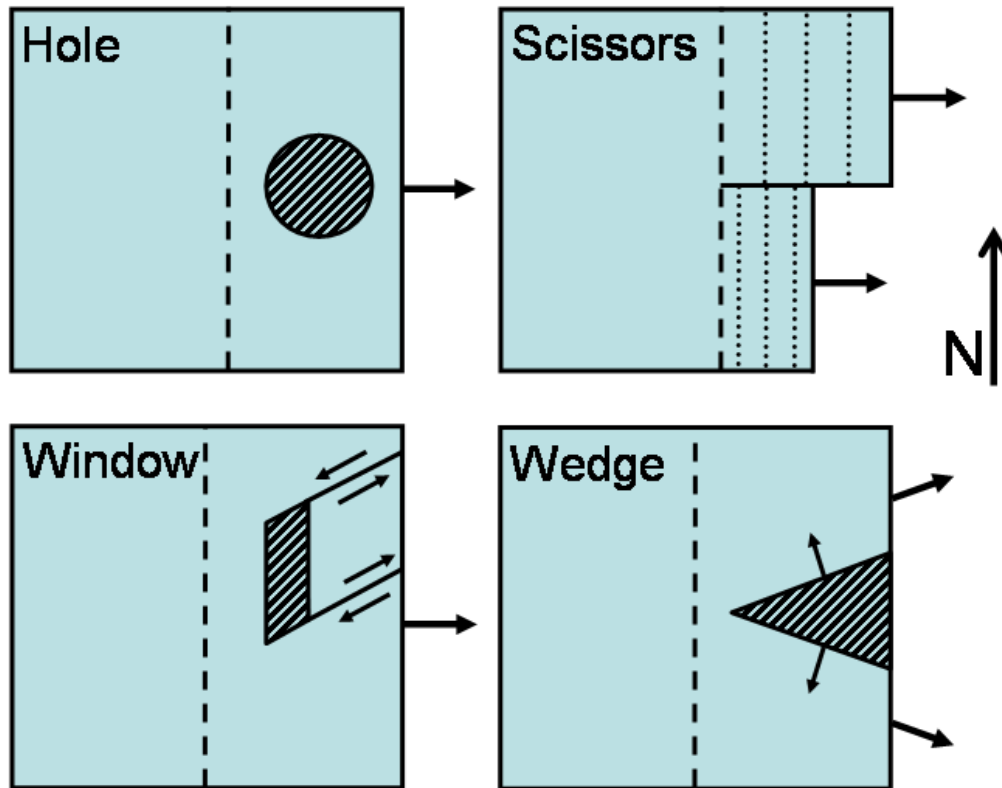


Figure 2.10: Four possible ways to create an opening in the slab through which the plume could pass: the “hole” caused by the plume itself; the “scissors”-style contour perpendicular tear as suggested by *Cahill and Isacks* [1992] with the south side dipping more steeply than the north side; the “window” opening initiated by contour-parallel normal faulting; and the “wedge”-style ripping in which the slab is pulled laterally apart. Cross-hatching indicates missing slab; dashed lines indicate the slab hinge; dotted lines indicate slab contours; large arrows indicate down-dip direction; small arrows indicate slab motion or relative motion.

contours are shown green on Figure 2.9(a) and are based on the CHARGE array [2000 – 2003] events plotted as small diamonds. North of 33° S we use the 100, 110 and 120 km contours of *Linkimer Abarca* [2011] shown light blue on Figure 2.9(a). *Linkimer Abarca* [2011] uses the SIEMBRA (2007 – 2009) and ESP (2008 – 2010) arrays and has considerably more events (not shown) north of 31° S. These result in substantially different contours in the flattest portion of the slab, that are quite consistent with the EHB events that are plotted.

South of 37° S we use the 110, 150 and 170 km contours colored magenta on Figure 2.9(a). They are contours of a plane fit to EHB events shown as a map in Figure 2.9(b) and in cross-section in Figure 2.9(c). The strike of this plane is determined to be 10.75° E of N at 39° S. The 110 km contour is seen to be almost exactly along the volcanic front, a coincidence which strengthens our result. Parallel planes +10 and -10 km from the best-fitting plane bound the scatter. However 18 events are not enough to decide whether this scatter represents the actual thickness of the seismogenic zone or statistical uncertainty. We simply use the best-fitting plane to estimate the slab surface because we are a long way from the flat slab region of primary interest and a 10 km error is of little consequence to our goal.

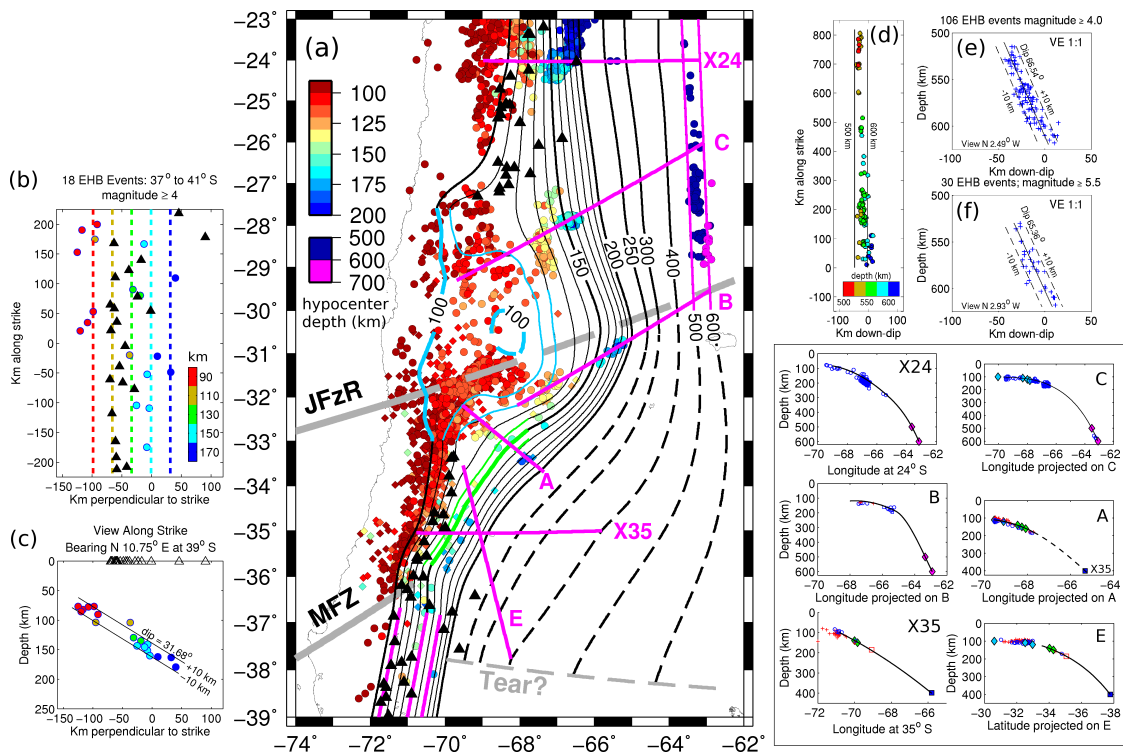
To constrain the deeper parts of the slab, we transformed EHB hypocenters deeper than 500 km, 21.7° to 29° S and west of 62.5° W to cartesian coordinates that correct for Earth's curvature. Figure 2.9(d) and 2.9(e) show map and along-strike views of the plane that best fits the events with magnitude 4.0 or greater. Planes +10 and -10 km from and parallel to the best-fitting plane in Figure 2.9(e) define a tablet that again bounds the scatter. The number of events is much larger than in Figure 2.9(c). The distribution appears relatively uniform across the thickness of this tablet and has abrupt edges. This argues that the spread of hypocenters is not simply statistical inaccuracy but may be due to a seismogenic zone about 20 km thick. Figure 2.9(f) shows the cross-section when the magnitude cutoff is increased to 5.5. The strike direction has changed less than 0.5° and the dip by only slightly more than

1°. Otherwise the impression remains that the events are fairly uniformly distributed throughout the thickness of a 20 km thick tablet. We use the plane displaced +10 km as our best estimate of the slab top. The 500 and 600 km contours from 23° S and linearly extrapolated from 29° S to 30° S set the deep slab boundary condition. These contours are highlighted with magenta on Figure 2.9(a).

Finally, slab depths at approximately 10 km intervals along six transects labelled A, B, C, E, X24 and X35 on Figure 2.9(a) were added. The individual transects in cross-sections with 1:1 vertical exaggeration are shown in the box together with the data used to determine the constraint curves. Unlike typically plotted transects, only hypocenters within $\pm 0.1^\circ$ (about 11 km) are projected onto each transect. This reduces bias associated with cross-transect slab geometry. Transects A, B, C and X24 were chosen to maximize the number of events deeper than 150 km. Transects X35 and E coincide with seismic tomography model slices of *Pesicek et al.* [2012].

Each constraint transect curve was constructed by fitting a 2nd or 3rd order polynomial above 200 km to the top of the envelope of events from the CHARGE and EHB catalogs and the intersections with the *Anderson et al.* [2007] and *Linkimer Abarca* [2011] contours. Each curve is extrapolated below 200 km using a cubic spline that is constrained by the curve above 200 km and several different constraints at depth. North of 30° S, the estimated 500 and 600 km contours set the slope of the deep slab. On X24, EHB events between 200 and 300 km are also used. On X35 and E, the position of the points at 400 km depth are estimated from the tomographic slices of *Pesicek et al.* [2012] which coincide with these transects. The 400 km deep point on E additionally coincides with down-dip extrapolation of the plane shown in Figure 2.9(b) and 2.9(c). Finally the extrapolation of constraint A below 200 km agrees with the 400 km point on X35 although the dashed portion of curve A deeper than 200 km is not used as a constraint.

Figure 2.11: (a) Contours of the minimum curvature surface fit to a series of constraints on the Nazca slab surface deeper than 100 km. Contours are dashed where less certain. Circles filled with color indicating depth are earthquakes with magnitudes ≥ 4.0 from the EHB catalog (1960 – 2008). Diamonds are events from the CHARGE catalog (2000 – 2003). Black triangles are geologically recent volcanoes. JFzR = Juan Fernandez Ridge; MFZ = Mocha Fracture Zone. Constraints on the slab surface consist of: (1) light blue contours from *Linkimer Abarca* [2011]; (2) green contours from *Anderson et al.* [2007]; (3) magenta contours south of 37° S estimated by fitting a plane to EHB events as shown in (b) and (c); (4) magenta 500 and 600 km contours north of 30° S estimated by fitting a plane to deep EHB events from 21.7° S to 29° S as shown in (d), (e) and (f); and (5) six magenta transects along which slab depth has been estimated at about 10 km spacing. Deep earthquakes with magnitude ≥ 4.0 color-coded with their depth are plotted in (d). The 500 and 600 km contours of the best-fitting plane are shown. Their cross-section viewed along strike is shown in (e). The cross-section (f) repeats the fit using only events with magnitude ≥ 5.5 . The data used to construct the transects A, B, C, E, X24 and X35 are summarized in 1:1 cross-sections in the box. Crosses are CHARGE events within $\pm 0.1^\circ$ of the transect; circles are EHB events within the same windows; diamonds are intersections with constraint contours filled with contour color; open squares on transect B are Moment Tensor Centroids; the dark blue filled squares at 400 km on A, E and X35 are estimated from the seismic tomographic slices of *Pesicek et al.* [2012]; the open squares on E and X35 are at the intersection of these two transects. The point labeled X35 on transect A is also on X35. The dashed portion of curve A is not used as a constraint. Finally, the termination of the Nazca slab in a “Tear” at about 38° S is from *Pesicek et al.* [2012].



2.10 Acknowledgments

This project is supported by the U.S. National Science Foundation (NSF) Grants EAR9909390, EAR0310113 and EAR0739116 and U.S. Department of Energy Office of Basic Energy Sciences grant DE-FG03-99ER14976. MT equipment is from the EMSOC Facility supported by NSF Grants EAR9616421 and EAR0236538. This project also received support from the Agencia Nacional de Promoción Científica y Tecnológica PICT 2005 No. 38253. The first author received support from the Seattle Chapter of the ARCS Foundation, and from Graduate Research Support, Qamar, Stephens, and Coombs Fellowships provided by the Dept. of Earth and Space Sciences, University of Washington. Thank you to Jimmy Larsen for numerous helpful discussions. Gabriel Giordanengo of Instituto de Geocronología y Geología Isotópica provided extensive assistance in the field. Thank you to Paul Bedrosian for a constructive review.

Chapter 3

**THREE-DIMENSIONAL ELECTRICAL CONDUCTIVITY
IN THE MANTLE BENEATH THE
PAYÚN MATRÚ VOLCANIC FIELD
IN THE ANDEAN BACK-ARC OF ARGENTINA
NEAR 36.5 S**

3.1 Authors

- Aurora I. Burd and John R. Booker, Department of Earth & Space Sciences, University of Washington, Seattle, Washington, USA.
- Randall L. Mackie, Land General Geophysics, CGG, Milan, Italy.
- Alicia Favetto and M. Cristina Pomposiello, Instituto de Geocronología y Geología Isotópica, Universidad de Buenos Aires, CONICET, Buenos Aires, Argentina.

3.2 Publication Information & Note

The remaining text in this chapter will be submitted to *Geophysical Journal International*.

This paper's region of study is the Payunia Basaltic Province. There are multiple names referring to all or part of this region, including "Payunia", "Payenia", "Andino-Cuyana Basaltic Province", "Mendoza Retroarc Volcanic Province", "Payún Matrú Volcanic Field", and "Complejo Efusivo Neógeno."

3.3 Summary

Southern Mendoza and northern Neuquén Provinces, south of the Pampean Shallow Subduction region in western Argentina, are host to the < 2 Ma Payunia Basaltic Province, which covers $\sim 39,500$ km² with primarily basaltic intraplate volcanism. This back-arc igneous province is the result of extension due to trench roll-back following steepening of a flat slab that existed in the middle to late Miocene. Magnetotelluric data collected in 2005 and 2008 at 37 sites from $67 - 70^\circ$ W and $35 - 38^\circ$ S are used to probe the source of the Payún Matrú basalts. These data, which require significantly 3D structure, were used in a 3D non-linear conjugate gradient inversion. We identify two significant electrically conductive structures. One, called the SWAP (shallow western asthenospheric plume) approaches the surface beneath the Caldera Payún Matrú & the Volcán Trómen and dips westward toward the subducted Nazca slab. The second, called the DEEP (deep eastern plume) approaches the surface ~ 100 km to the southeast and dips steeply east to 400 km depth while remaining above the subducted Nazca slab. We used a variety of model assessment techniques including both forward modeling and additional inversion to test the veracity of these features. We interpret the SWAP as the source of the < 2 Ma intraplate volcanism. Our inversion model assessment suggests that the SWAP does not need to connect to the Nazca slab. This is compatible with the lack of recent arc signature magmatism near Payún Matrú. The SWAP and DEEP are electrically connected only in the shallow crust, which is likely due to the Neuquén sedimentary basin and not a magmatic process. We propose that the SWAP and DEEP may have been more robustly connected in the past, but that the DEEP was decapitated to form the SWAP when shallow north-westward mantle flow resumed during steepening of the slab. The ~ 2 Ma basaltic volcanism results from SWAP magma that had ponded below the crust until extension allowed eruption. The westward dipping portion of the SWAP is interpreted as mantle shear in the renewed mantle corner flow – this

explains why the SWAP and Nazca slab can appear connected, yet there is no recent arc-signature magma in this region.

3.4 Geologic Background

The Payunia (sometimes called Payenia) Basaltic Province (PBP) in the northern Neuquén basin of Argentina near (36.5° S, 69.5° W, see Figure 3.1) is a fascinating but little-studied region. This part of the Andean back-arc is south of the Pampean Shallow Subduction region near 31.5° S [Cahill and Isacks, 1992; Anderson *et al.*, 2007; Linkimer Abarca, 2011] and subduction is a more normal 36° [Pesicek *et al.*, 2012].

The present-day PBP spans $\sim 39,500$ km² of southern Mendoza and northern Neuquén provinces and lies in the Andean back-arc approximately 150 km east of the main Andean Southern Volcanic Zone (SVZ) [Ramos and Folguera, 2011]. The PBP is usually divided into several sections including the Payún Matrú Volcanic Field (PMVF) which includes the area shown in browns on Fig. 3.1(b) and the area shown in gray to its west and south-east, the Llanquanelo and Cerro Nevádo Volcanic Fields in gray to the north of the PMVF, the Auca Mahuida Volcanic Field shown in light gray just south of the Rio Colorado, and the Tromen Volcanic Field shown in dark gray south-west of the PMVF.

The volcanics straddle two basement terranes: Cuyania and Chilenia. Cuyania is a sliver of Laurentia and Chilenia less certainly also from North America which were accreted to Gondwana in the Ordovician or Devonian [Ramos, 2010]. Payun Matru sits atop Chilenia; Cerro Nevado (see Fig. 3.1(b)) is on the San Rafael Block along the southwestern edge of Cuyania. Over the basement lie the Mesozoic rocks of the Neuquén Basin (outlined in Fig. 3.1(b)) [Howell *et al.*, 2005]. Finally, foreland units associated with the Andean Orogeny [Ramos, 1999] are up to 2 km deep along the Rio Grande west and northwest of Payun Matru, but mostly much less.

Payunia has a complicated geologic history, but we are interested in only the last

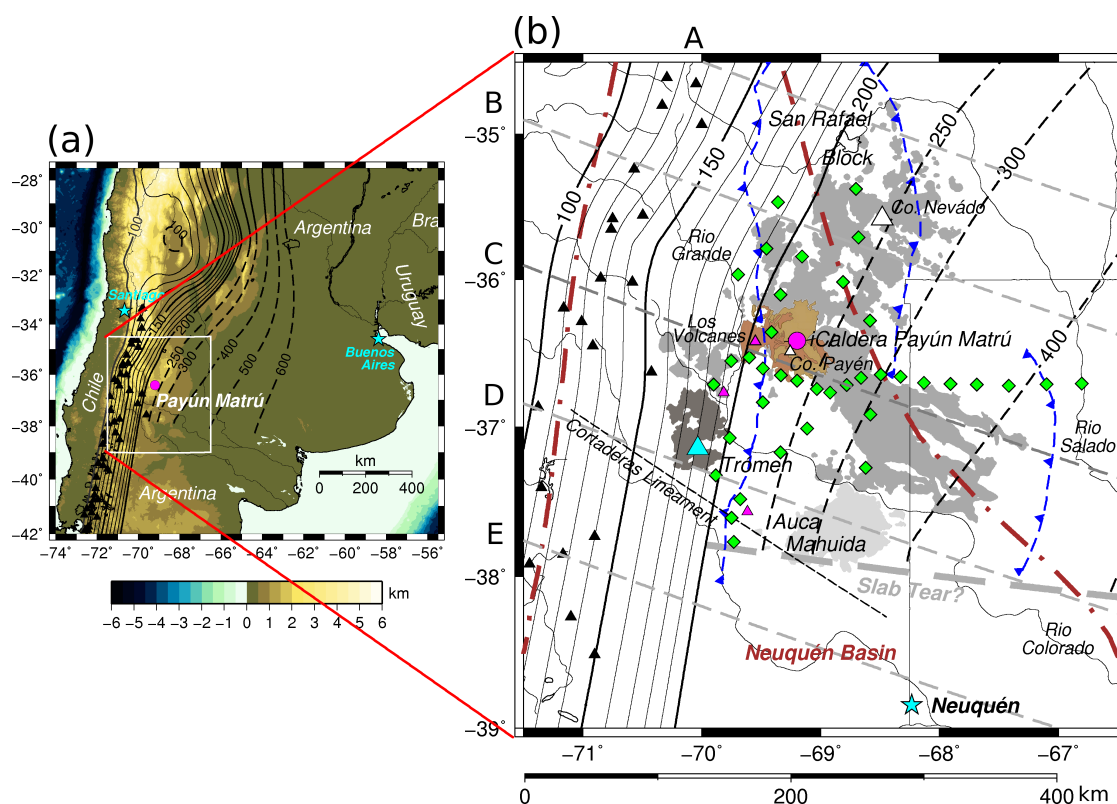


Figure 3.1: (a) Topography of South America, with study region in white box, active Andean Southern Volcanic Zone (SVZ) volcanoes as black triangles, Caldera Payún Matrú as a magenta circle, and contours of subducted slab (after *Burd et al.* [2013]) in black, with uncertain slab locations indicated with dashed black lines. (b) Payunia region, showing MT sites as green diamonds, active Andean Southern Volcanic Zone volcanoes as black triangles, Caldera Payún Matrú as a magenta circle, Volcán Trómen as a cyan triangle, Cerro Payén as a small white triangle, and Cerro Nevádo as a large white triangle. There are three small pink triangles representing geologically young activity: one is the Los Volcanes region and the other two are single monogenetic centers. Distribution of volcanics and faults is based on *Ramos and Folguera* [2011]. The Mesozoic Neuquén Basin is outlined in brown dash-dot curves [*Howell et al.*, 2005] and the basement thrust faults bounding the Proterozoic San Rafael Block are in blue dashed curves. The ~ 1.7 Ma basaltic volcanism of the Payunia region (including the Llanquanelo Volcanic Field that includes Cerro Nevádo) is in gray, with the 1.8–1.6 Ma Trómen Volcanic Field shown in darker gray and the 2–0.8 Ma Auca Mahuida Volcanic Field shown in light gray. The PMVF volcanic products younger than 200 ka are shown in tan. The Cortaderas Lineament aligns with the southern extent of the < 2 Ma volcanism, but is considered by *Kay et al.* [2006] to be the southern limit of a Miocene shallow subduction region. The slab tear deeper than 200 km based on tomography by *Pesicek et al.* [2012] is a heavy gray dashed line. Thin gray dashed lines A – E represent transects discussed in the Results section of this paper. The transects are rotated 20° clockwise to match the inversion grid, so that “North” within the grid is N20E in geographic coordinates.

20 Ma. *Kay et al.* [2006] summarize the data supporting a shallower slab and arc influenced volcanism from 20 – 5 Ma. They and *Folguera et al.* [2006] argue that the back-arc PBP is the result of extension due to trench roll-back and steepening of this Miocene shallow slab. *Ramos and Kay* [2006] conclude that the slab's steepening throughout the Pliocene and Quaternary heralded the eruption of much of the PBP's basaltic lava: during this time, the percentage of mantle melting appears to have increased and the subduction influence on the geochemistry has declined [*Kay et al.*, 2006]. However, a recent tomographic study by *Pesicek et al.* [2012] did not image the present-day Nazca slab deeper than 200 km south of 38° S. The compiled contours of the subducted Nazca slab [*Burd et al.*, 2013] are shown in Fig. 3.1.

Volcanism in the PMVF near the Caldera Payún Matrú has been active for roughly the last 2 Ma [*Ramos and Folguera*, 2011]. *Germa et al.* [2010] date the Cerro Payén stratovolcano to 0.275 Ma. The Payún Matrú shield volcano collapsed to form a caldera sometime between 0.168 Ma and 0.082 Ma and is henceforth referred to as Caldera Payún Matrú [*Germa et al.*, 2010]. This volcano lost 25 km³ of its total 240 km³ during its caldera-forming eruption.

There are more than 800 volcanic vents and small cinder cones in the PBP, which have essentially no arc signature and are primarily alkalic [*Bermúdez et al.*, 1993; *Inbar and Risso*, 2001b]. Recent work by *Germa et al.* [2010] indicates that the group of vents and cinder cones known as Los Volcanes to the west of the Caldera Payún Matrú range in age from ~28 ka to younger than 7 ka and identify these lavas as basaltic to trachybasaltic. Measurements of the degradation of the shapes of these cinder cones suggests that the most recent eruption may have been about 1,000 years ago [*Inbar and Risso*, 2001b]. Based on the oral traditions of the indigenous inhabitants, *Inbar and Risso* [2001a] suggest that the most recent eruption could have been between 1000 and 200 years ago. Inside the Caldera Payún Matrú, *Germa et al.* [2010] identify trachytic lavas ranging in age from 37 ka to 7 ka. Thus, although the magma production rate is presently low, production of both basaltic and more

evolved magmas almost certainly continues today. For a more comprehensive overview of Payunia, see *Ramos and Folguera* [2011].

The PBP volcanism is geochemically similar to intraplate basalts erupted from mantle sources undepleted of lithophile elements. These melts are often considered to arise from below the bottom of the mantle transition zone (MTZ) which spans 410 – 660 km. *Bercovici and Karato* [2003], however, argue that this type of volcanism need only come from the top of the MTZ. They suggest that the initial melting that strips out incompatible elements is the result of the phase change of hydrous minerals such as wadsleyite to olivine as mantle material moves upwards through the 410 km discontinuity.

Evidence that the PBP magmas have passed quickly through the crust comes from near-surface geology. Extensional features in the PBP include reactivated normal faults [*Kay et al.*, 2006] and the relatively shallow Moho identified by *Gilbert et al.* [2006]. *Hernando et al.* [2012] state that the PBP flows have $^{87}\text{Sr}/^{86}\text{Sr}$ values “suggesting little contamination with radiogenic crust.” In addition, *Folguera et al.* [2009] also argue against a near-surface basaltic reservoir, stating that the wide distribution of monogenetic cones means that each eruption has created its own path to the surface. It is thus reasonable to conclude that the Payún Matrú source is relatively deep and interacts very little with the crust while approaching the surface.

3.5 Methods

The magnetotelluric method uses passively recorded electric and magnetic field data at Earth’s surface to probe electrical conductivity below Earth’s surface. Electrical conductivity (with units of Siemens per meter) is strongly sensitive to changes in phase (which depends on temperature and pressure), water content, and melt fraction, but between roughly 100 and 400 km depth, elevated conductivity of upper mantle minerals are more likely the result of partial melt or other interconnected fluids than hydrous minerals [*Yoshino et al.*, 2009]. Because conductivity at dry upper mantle

conditions is $\ll 1$ S/m, it is usual to use its reciprocal, resistivity (with units of Ohm-m).

Figure 3.1(b) shows the location of 37 MT sites collected in two field campaigns. The east-west profile was collected in 2005, while the broader array was filled out in 2008. Each site recorded 5 to 15 days of 3-component magnetic field (\mathbf{H}) and horizontal components of electric field (\mathbf{E}) sampled at 0.25 s with Narod Intelligent Magnetotelluric Systems (NIMS). The electric field dipoles used Pb-PbCl₂ electrodes [Petiau, 2000].

In the frequency domain \mathbf{E} and \mathbf{H} are related by

$$\mathbf{E} = \begin{bmatrix} E_x \\ E_y \end{bmatrix} = \mathbf{Z}\mathbf{H} = \begin{bmatrix} Z_{xx} & Z_{xy} \\ Z_{yx} & Z_{yy} \end{bmatrix} \begin{bmatrix} H_x \\ H_y \end{bmatrix} \quad (3.1)$$

where the impedance tensor \mathbf{Z} is a function only of the sub-surface electric conductivity structure. The time-stationarity of \mathbf{Z} allows one to estimate it using non-stationary time series of \mathbf{E} and \mathbf{H} . The frequency domain relation between the vertical and horizontal components of the magnetic field

$$H_z = \mathbf{W} \cdot \mathbf{H}_{horiz} = \begin{bmatrix} W_x & W_y \end{bmatrix} \begin{bmatrix} H_x \\ H_y \end{bmatrix} \quad (3.2)$$

defines the ‘‘induction vector’’ \mathbf{W} . If the polarization of the source \mathbf{H} is sufficiently random, \mathbf{W} also depends only on the sub-surface structure. \mathbf{Z} and \mathbf{W} have been estimated at periods from 3 to 10^4 s using the robust multi-station algorithm of Egbert [1997]. All sites are processed identically so that they are directly comparable. \mathbf{Z} and \mathbf{W} are complex and together provide 12 data at each period and site. Only 9 periods from 20 to 5120 s are used in this study.

For the purposes of this paper, the basement rocks of the Chilenia and Cuyania Terranes are important only in that they are quite resistive (> 100 Ohm-m). The skin depth (km) for penetration of electromagnetic energy is given by $\delta = 0.5\sqrt{\rho T}$

where ρ is resistivity and T is period (s). Energy with 10^3 s period penetrates 150 km through 100 Ohm-m material. The sedimentary units of the Neuquén Basin and Rio Grande foreland basin are more conductive (of order 10 Ohm-m), but the skin depth of 10 Ohm-m material at 20 s period is 7 km and substantially exceeds the maximum combined sedimentary cover. The top of the mantle is expected to have resistivity approaching 10^3 Ohm-m, decreasing to about 100 Ohm-m just above the MTZ [Yoshino *et al.*, 2012]. Basaltic melt is much more conductive (1 Ohm-m or less) and mantle containing a few percent of interconnected partial melt is at least an order of magnitude less resistive than the surrounding mantle [Schilling *et al.*, 1997]. In summary, with 20 to 5120 s data we can expect to image low resistivity materials such as partial melt in the mantle to depths of 300 km or more [Booker *et al.*, 2004].

The magnitudes of the elements of \mathbf{Z} can be significantly affected by small scale, unresolvable structure that distorts interpretation of regional structure. The most common form of this distortion is the result of electric charges that accumulate where current flows along shallow conductivity gradients. When these charges are in-phase with the regional electric field, the distortion is called “static” or “Galvanic”. Caldwell *et al.* [2004] introduced a function of the impedance

$$\Phi = (Re(\mathbf{Z}))^{-1} Im(\mathbf{Z}) = \begin{bmatrix} \Phi_{xx} & \Phi_{xy} \\ \Phi_{yx} & \Phi_{yy} \end{bmatrix} \quad (3.3)$$

that is unaffected by static distortion. Φ is called the “impedance phase tensor” or simply the phase tensor. Its four elements are real and it has a preferred coordinate system in which these four data can be transformed to the direction of an ellipse axis, lengths of the ellipse semi-axes and an angle

$$\psi = \tan^{-1} \left(\frac{\Phi_{xy} - \Phi_{yx}}{\Phi_{xx} + \Phi_{yy}} \right) \quad (3.4)$$

called the “normalized phase tensor skew” [Booker, 2013]. ψ is rotationally invariant and can be computed from \mathbf{Z} in any coordinate system. (Note that ψ is twice the

skew angle β defined by *Caldwell et al.* [2004]).

If the regional structure is 2D, $\psi = 0$, the phase tensor ellipse is aligned with the strike and the ellipse semi-axes are the tangents of the phases of the off-diagonal elements of the regional (i.e.undistorted) impedance. If ψ is not zero, the regional structure must be 3D. $|\psi| > 6^\circ$ is a good working criterion for concluding that the data must be 3D [*Booker*, 2013]. $|\psi| < 6^\circ$ can be considered “quasi-2D”, but may still be 3D. Fig. 3.2 shows maps (to be referred to as “polka-dot plots”) of ψ at our 37 sites. Data that meet the quasi-2D criterion of $|\psi| < 6^\circ$ are coloured green. The error bars for ψ are typically much less than 6° (see *Booker* [2013] for examples). It is quite clear that a preponderance of sites cannot be considered quasi-2D and thus require 3D interpretation.

Ideally, we would have incorporated the phase tensor into our inversion. However, because 3D inversion of the phase tensor is not yet sufficiently developed, we invert \mathbf{Z} and \mathbf{W} directly for shallow 3D structure that fits features in the data that can be the result of static distortion. However, because our site spacing is often larger than the structures causing the distortion, the details of this shallow structure are expected to be less reliable than deeper structure.

We invert the real and imaginary parts of all elements of \mathbf{Z} and \mathbf{W} using a 3D Non-Linear Conjugate Gradient (NLCG) algorithm ([*Mackie et al.*, 2001; *Mackie and Watts*, 2012; *Rodi and Mackie*, 2012]). This seeks a model that minimizes the objective function,

$$S = \chi^2 + \tau R(m) \quad (3.5)$$

where τ is the trade-off parameter, $R(m)$ measures the “roughness” of the model m (also called the “structure penalty”), and

$$\chi^2 = \sum_{i=1}^N \frac{r_i^2}{\sigma_i^2} \quad (3.6)$$

is a measure of the data misfit. r_i^2 are the squares of the data residuals (i.e. predicted

values – observed values), σ_i^2 are the variances, and N is the number of data.

Roughness $R(m)$ can be defined as the square of the Laplacian of the model, averaged over the model. However, because spatial resolution decreases with depth due to the diffusive physics of MT, we modify this definition so that the structure penalty in all spatial directions increases with depth. For additional discussion of $R(m)$ see *Burd et al.* [2013].

All models terminate in a 3 Ohm-m half-space deeper than 660 km. A deep resistivity of this order is widely accepted based on mantle conditions and minerals [*Xu et al.*, 2000]. Furthermore, *Xu et al.* [1998] find the phase change from olivine to wadsleyite (which occurs at roughly 410 km depth) corresponds to a two order of magnitude decrease in resistivity. *Yoshino* [2010] also documents a decrease in resistivity of at least an order of magnitude at 410 km. Thus there is a geophysical reason to permit a resistivity jump at 410 km. Therefore in addition to an $R(m)$ computed for the entire model, we have also performed inversions in which $R(m)$ has a tear at 410 km at which the vertical gradient of the model across this tear is excluded from computation of the roughness.

The inversions include electrically conductive oceans. They are in a coordinate system that has been rotated 20° east from geographic north to align the grid more closely to the strike of the Pacific Coast and subducted slab (see Fig. 3.1(a)). The importance of the Pacific Ocean in 2D inversions of our data was shown by *Booker et al.* [2005] and the importance of including both Pacific and Atlantic Oceans in 3D is discussed by *Burd et al.* (manuscript in preparation, 2013). In order to keep the mesh size relatively small while accurately modeling the effect of ocean bathymetry, we used an ocean of constant depth but varying electrical conductance. (Conductance [Siemens] = layer thickness [m] \div electrical resistivity [Ohm-m].) This layer has high resistivity when the water is shallow, and low resistivity when the water is deep. The ocean layers and the discontinuity between land and water are excluded from the $R(m)$ computation.

Instead of χ^2 it is common to report the “normalized RMS”,

$$nRMS = \sqrt{\frac{\chi^2}{N}} \quad (3.7)$$

where the $nRMS$ would be 1.0 if each datum had a misfit equal to its estimated error.

Our algorithm uses weighted least squares. Data with error estimates σ_i smaller than a threshold called the “error floor” are weighted equally while data with larger error estimates are down-weighted. This weighting scheme is implemented by increasing estimated uncertainties below the error floor up to the floor. Henceforth, σ_i refers to estimated data error after the error floors have been applied.

Since we are inverting the real and imaginary parts of the impedance elements, error floors are applied to these 8 data equal to 2% of the magnitudes of the off-diagonal elements $|Z_{xy}|$ and $|Z_{yx}|$. The error floors for the diagonal elements are set equal to that of the off-diagonal element in the same row. This is reasonable if the noise is primarily in the electric field. An absolute error floor of 0.01 is used for the 4 real and imaginary parts of the induction vector \mathbf{W} .

These error floors are lower than commonly used for 2D inversion. 2D inversions invert apparent resistivity (related to $|\mathbf{Z}|$) and phase of off-diagonal elements. Our floors are equivalent to 4% for the apparent resistivities and 1.2° for the impedance phase. However, our inversion can still achieve $nRMS$ values close to 1.0, a rare occurrence in 2D inversions even with larger error floors. This is because 3D effects in data treated as 2D can be thought of as noise. Larger misfits must be tolerated in 2D inversions to prevent a minimum structure algorithm from generating spurious structure due to fitting this “3D noise”.

3.6 Results

Figure 3.3 is a “trade off” diagram of $nRMS$ versus $R(m)$ for a series of 3D inversions done with decreasing values of τ in the objective function (Eq. 3.5). Each model is started from a smoother model with larger τ . This strategy guards against introducing

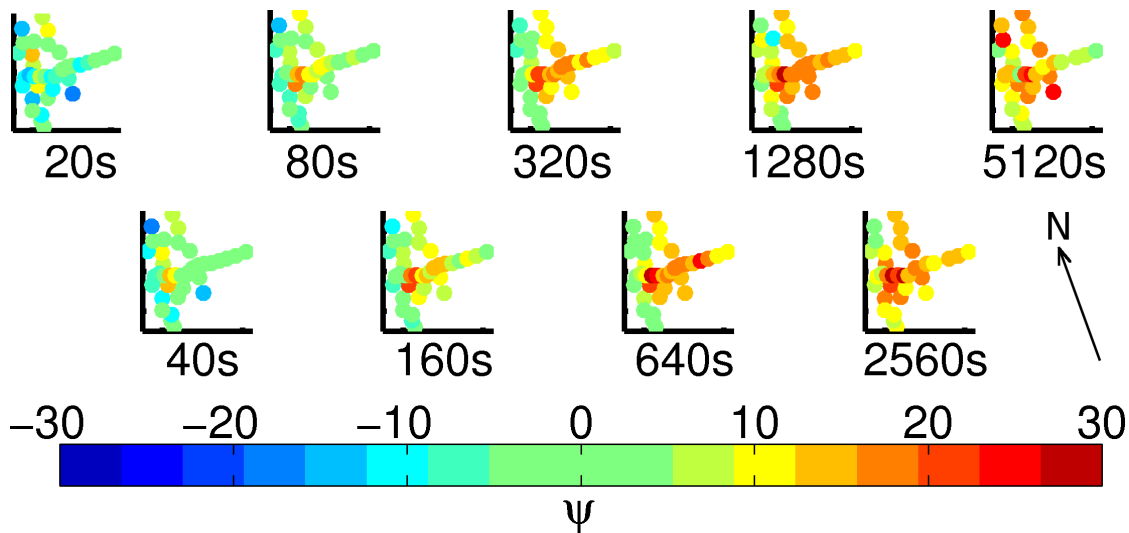


Figure 3.2: Plots of normalized phase tensor skew angle, ψ for observed data for all sites, at each period used in the inversion. $|\psi| < 6^\circ$ is compatible with 2D interpretation (shown in green in this figure), so most sites are clearly significantly 3D. North arrow is indicated because inversion grid (and all subsequent analyses) is rotated 20° west of N.

unnecessarily rough structure in early iterations because NLCG algorithms typically require a large number of iterations to remove such structure at later iterations. Also, in our experience a path through model space to an ultimately smooth model by way of much rougher models has a higher probability of being caught in local minima of the objective function.

The trade-off curve is initially steep but levels out as $nRMS$ decreases. It is below 1.0 for the roughest model p208 ($\tau = 0.003$). This model has small scale structure that we judge geologically unlikely and we have not attempted to lower the misfit further. Models p205 to p207 share all major features. We have chosen to interpret model p207 as the best compromise between increasing the resolution while guarding against structural artifacts due to fitting noise. Polka dot plots of the $nRMS$ by site and period are shown for p207 in Figure 3.4. We see that the misfits are fairly “white” (distributed uniformly with space and period) except at the shortest period.

It is not surprising that the misfit is larger at the shortest period because we do not have enough site density to accurately model the very shallow structure.

“Fence” plots with nominally east-west slices of model p207 are shown together with two resistivity isosurfaces in Figure 3.6(a – c) (note that Fig. 3.1(b) shows slices A – E, which are rotated 20° clockwise from east-west to match the inversion grid, so that “North” within the grid is N20E in geographic coordinates). We focus on two major features: (1) a conductive structure visible in slices B, C, and D that dips steeply eastward just above the Nazca slab to near the top of the transition zone at 400 km, which we call the DEEP (DEep Eastern Plume); and (2) a conductor visible in slices C and D that dips westward to meet the subducted slab at about 150 km. We call this structure the SWAP (Shallow Western Asthenospheric Plume). The DEEP and SWAP are separated by a resistive zone roughly 100 km wide at most depths.

The details of the SWAP are best seen in the smaller scale resistivity isosurface (Fig. 3.6(c)). It appears to have a foot on the slab and then rises to a conductive body with significant north-south extent near the top of the mantle. This north-south structure has two obvious protrusions from its top. One rises directly up into the shallow crust under Caldera Payún Matrú (shown as a magenta circle in Fig. 3.6(b – c)). The second rises up close to the geologically young Volcán Trómen (shown as a black triangle in Fig. 3.6(b – c)).

3.6.1 Model Assessment

Fig. 3.6(d) shows the results of inversion p402, which has a “tear” at 410 km depth. p402 is fully converged and shown as a green triangle on Fig. 3.3: the global $nRMS$ value is comparable to p207, but $R(m)$ can not be directly compared to the other inversions shown in the figure because $R(m)$ for p402 does not include values at the tear’s location. If the data were not sensitive to structure below the depth of the tear, the region below the tear would have resistivity values identical to the bottom boundary condition of 3 Ohm-m because that is the smoothest possible structure

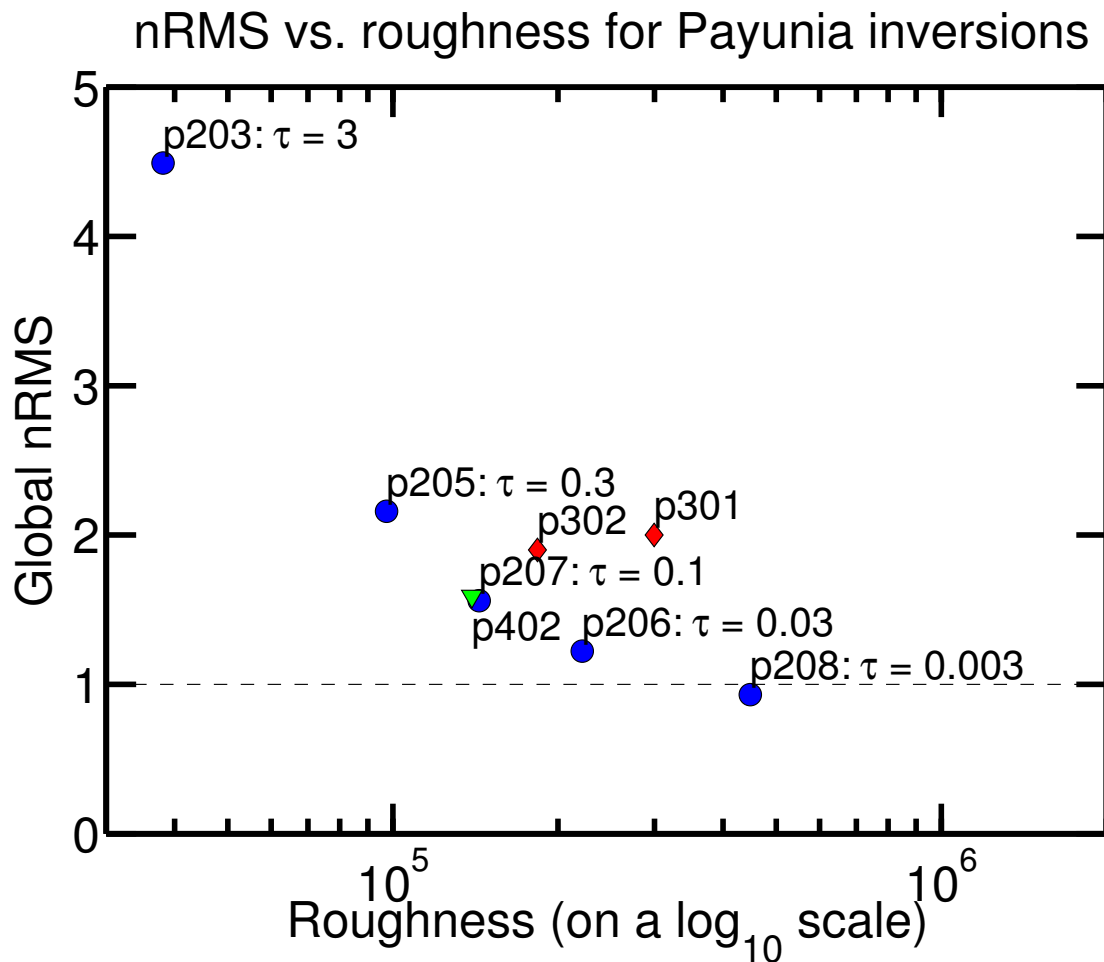


Figure 3.3: $nRMS$ versus roughness for Payunia inversions with different values of τ (the tradeoff parameter). Blue circles indicate the main inversion sequence, red diamonds are inversions using $\tau = 0.1$, which were used for hypothesis testing (discussed in Model Assessment section), and the green triangle is an inversion using $\tau = 0.1$ with a “tear” at 410 km depth (also discussed in Model Assessment section).

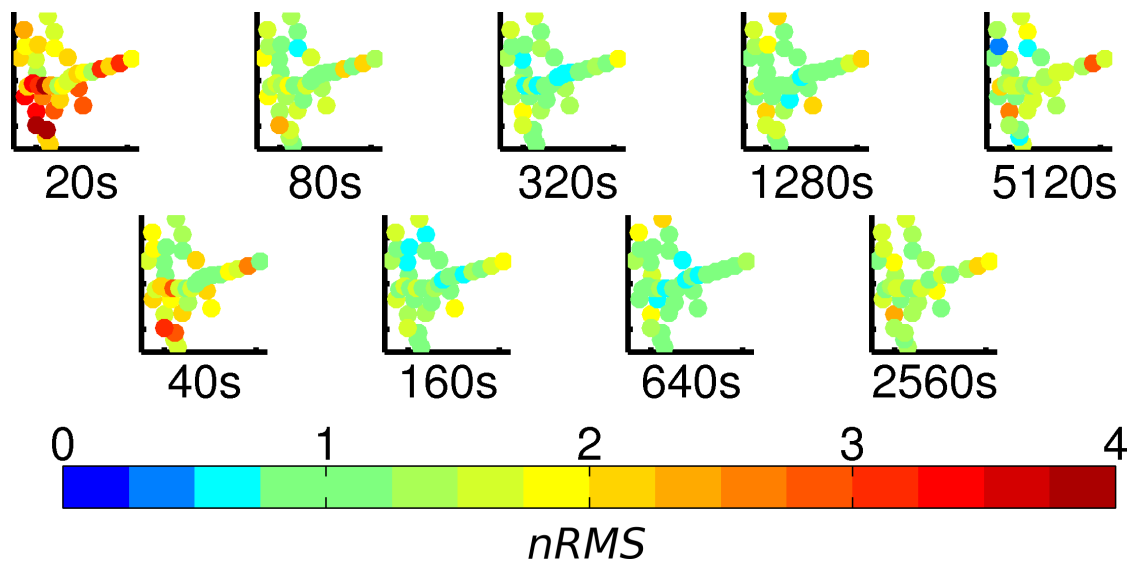


Figure 3.4: Maps showing $nRMS$ at each site at each period for p207. Site locations are indicated by the coloured circles, where the colour corresponds to the $nRMS$ at that site. Note that $0.75 < nRMS < 1.25$ are green to indicate sites at which the inversion was able to adequately fit the data. Note that the fit is spatially white: fit is equally good at all sites with no particular region being especially poorly fit. Fit is also approximately white by period with the exception of the larger $nRMS$ values at the shortest period. See text for discussion of why the misfit is not as good at the shorter periods.

below the tear. Structure below 410 km is visible in all slices, so the data are sensitive to structure below the depth of the tear. In addition, structure above the depth of the tear appears very similar to structure in p207. We conclude that upwards smoothing of the fixed bottom boundary has little effect on the model above 410 km.

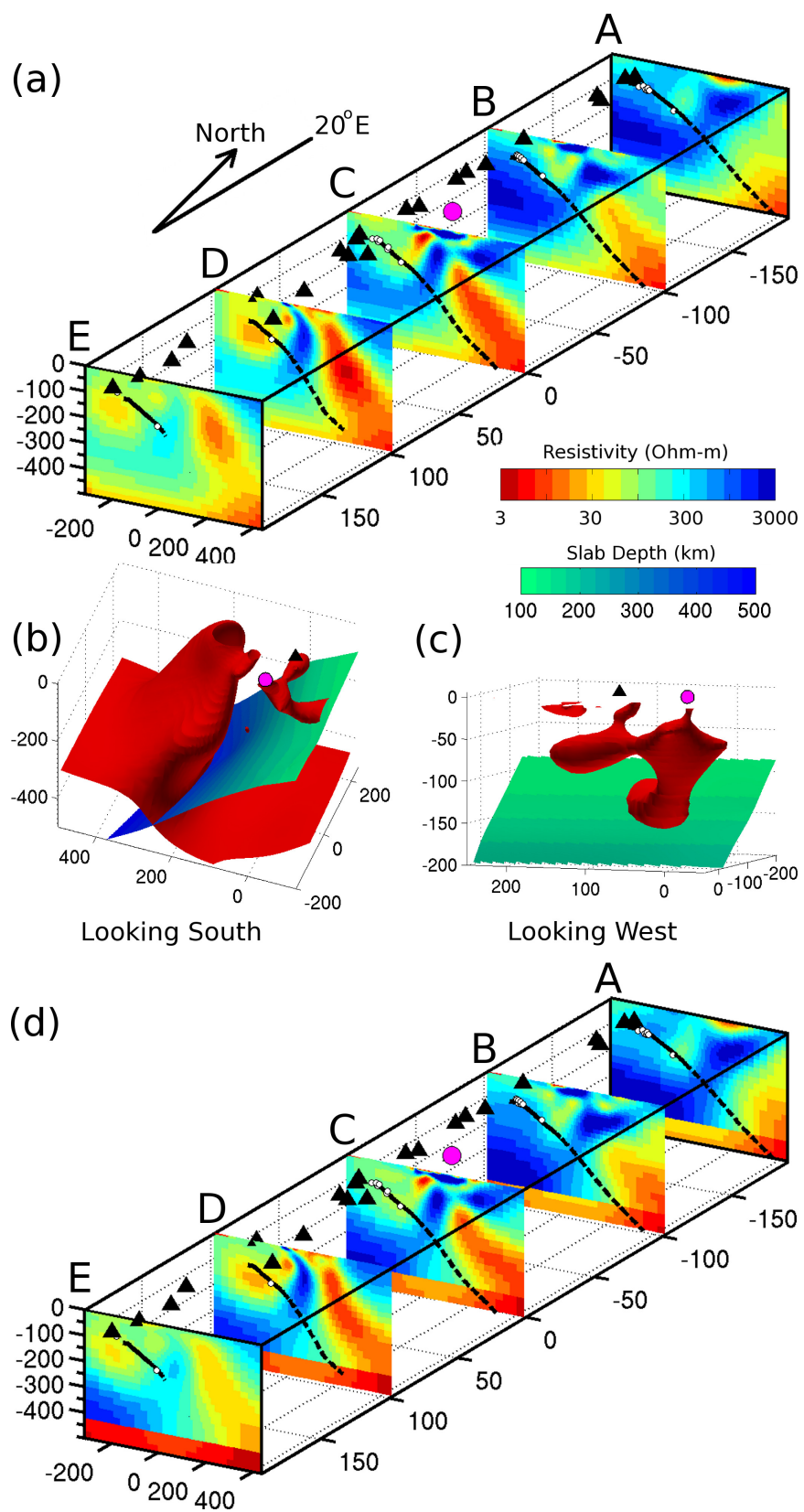
Seismologists commonly investigate resolution of their 3D inversions using “checkerboard” tests. Data are generated for a model consisting of an array of blocks alternating about the large scale average structure. These are inverted to see how well the blocks can be recovered. This is not as useful in our case because MT data respond most strongly to model features which constrain current to flow along extended continuous paths. An important by-product of this fact is that MT data can sense structure outside of an array.

In a sense, our inversions are already a resolution test because we find models that have the least complexity for given levels of data misfit. Thus the smallest spatial scales seen in the model tell you the resolution. An important caveat, however, is that this is only meaningful if you are not fitting data noise.

However, questions that need addressing include whether a given model feature is an artifact of the structure penalty used to define minimum structure and whether alternate models exist that have different structure but have the same value of the objective function (Eq. 3.5). Such models are often called “equifeasible”.

A model artifact that is constrained solely by the structure penalty will not alter the predicted data (within the measurement uncertainties) if the structure is removed. This is tested by removing structures and recomputing the predicted data. We can, however, go a step further and restart the inversion from the altered model constraining the region of removed structure to remain fixed. If the inversion cannot find a model with an objective function value as low as the original model, we have confidence that the structure is required. Our confidence will be even higher if this new inversion converges to a model that re-establishes current paths clearly similar to the original model given that it cannot use the region where the removed structure

Figure 3.5: (a) Nominally East-West slices of resistivity for inversion p207. Slice positions are shown on Fig. 3.1(b). Black triangles are Southern Volcanic Zone volcanoes active in the Holocene, magenta circle is location of Caldera Payún Matrú, black lines and dashed black lines are location of subducted Nazca slab, based on the slab surface discussed in *Burd et al.* [2013]. White points are earthquakes. Scale is stretched North-South to improve viewing. The origin $(0,0) = 69.5^\circ \text{ W}, 36.5^\circ \text{ S}$. X-axis and Y-axis are measured in km from this origin, and Z-axis is depth in km. (b) 35 Ohm-m isosurface of resistivity, showing DEEP to left and SWAP to right (in red), with subducted slab in green – blue. Volcán Trómen is the black triangle and Caldera Payún Matrú is the magenta circle. Isosurface is looking directly south and shows model deeper than 32 km (i.e. is mantle only). (c) shows only SWAP’s 35 Ohm-m isosurface, but has same legend as (b), except image looks directly west and model is not shown shallower than 8 km. (d) Nominally East-West slices of resistivity for inversion p402, which has a “tear” at 410 km depth (discussed in text). Same caption as Fig. 3.6(a).



existed. If this new inversion finds a model with an equal objective function, we have found an equifeasible model. If the the objective function is actually smaller for the new model, we can conclude that the original inversion was caught in a “local minimum” of the objective function.

We have identified two major structures that will be tested: the DEEP and the SWAP. For each we have performed three tests:

- (1). Remove the entire structure and re-converge the inversion while preventing the original structure from reforming.
- (2). Remove depth segments to find out which have significant influence on the data.
- (3). Block vertical current flow at specific depths to find out whether the structure must be electrically continuous.

Because the mantle background is approximately 100 Ohm-m, structure is removed by a thresholding scheme in which values below 100 Ohm-m are replaced by 100 Ohm-m. This allows the structure to cease to exist without creating new contrasting structure and reduces the model roughness.

Vertical current flow is blocked with thin horizontal 10000 Ohm-m tablets at the desired depths. These extend beyond the plume region that can be clearly identified as being less resistive than the background but not so far as to interfere with regional vertical currents associated with features like the oceans.

We are inverting 3996 data (12 responses at 9 periods at 37 sites). Judging the misfit changes for such a large number of data requires defining measures that are diagnostic and can be compactly presented. We use two characteristic ratios. The first is the ratio of $nRMS$ of the test model to its unperturbed value $nRMS_0$. For brevity, we write

$$P = \frac{nRMS}{nRMS_0} \quad (3.8)$$

The second is the absolute change in normalized phase tensor skew angle relative to its estimated error, which we write:

$$\delta\psi_\sigma = \frac{|\psi - \psi_0|}{\sigma} = \frac{|\Delta\psi|}{\sigma} \quad (3.9)$$

where σ is the estimated error of ψ with error floors applied. These are viewed as a function of period and site using the polka dot plots introduced in Fig. 3.2. Their more global values can be presented in tables (such as Table 3.6.1).

P is sensitive to data misfit in a way that would not depend on data error if all uncertainties were equal. $\delta\psi_\sigma$ is sensitive to changes in model dimensionality that affect the responses (as opposed to affecting only the roughness). When $P = 1$ there has been no change in $nRMS$, when $P < 1$ the $nRMS$ has decreased (unlikely, but still a possibility), and when $P > 1$ the $nRMS$ has increased. More importantly, when $P > 2$, it means that the misfit of every datum has on average doubled, which represents very significant worsening of the fit. When $\delta\psi_\sigma < 1$ then $\Delta\psi$ is insignificant relative to its error, when $1 < \delta\psi_\sigma < 2$ then $\Delta\psi$ is moderately in excess of its error, and when $\delta\psi_\sigma > 2$ then $\Delta\psi$ is at least twice the size of its error. P is useful because it includes both impedance tensor and vertical field data. If all data had the same errors, the error would cancel out of P and P would not depend on the error. In practice, however, data do not all have the same errors, but in our inversions, the error floors make the data errors similar in size and thus P depends only weakly on estimated error and choice of error floor. $\delta\psi_\sigma$ is useful because it is unaffected by shallow distortion, combines all elements of the impedance tensor and is sensitive to changes in structural dimensionality.

In polka dot plots, values of both ratios less than one are green because these values mean that the structural change is allowed by the data and thus we cannot assign geological importance to the structure being tested. We use the following P -test criteria to identify tests for which a change in structure has strongly affected the data: if $P > 1$ at many sites or $P > 2$ at a few sites, then we can be confident

that the original structure is not an artifact. Since $\delta\psi_\sigma$ is primarily related to the change in dimensionality of the model and the tests only change the structure near the DEEP or SWAP, we expect $\delta\psi_\sigma$ to be much more localized than P . Thus the following $\delta\psi_\sigma$ -test criteria identify tests for which the change in dimensionality of the structure is considered significant: $\delta\psi_\sigma > 1$ at many sites or $\delta\psi_\sigma > 2$ at a few sites.

Tests 1 (a & b): Existence of the Plumes

Figure 3.6 shows polka dot plots of P at all periods when the DEEP and SWAP are removed from model p207. P is greater than 2 across most of the spectrum with the changes peaking over each plume and at longer periods for the DEEP. 1280 s is strongly affected for both structures and to simplify discussion we present only this period for other tests. Table 3.6.1 further characterizes the distribution of misfit at 1280 s. Based on Table 3.6.1, there is only one site with $P < 2$ for removal of the DEEP and only 10 sites with $P < 2$ for the SWAP.

Figure 3.7 shows $\delta\psi_\sigma$ at 1280 s. The region of $\delta\psi_\sigma > 2$ is more spatially concentrated than P , but is still large at a significant number of sites.

Figure 3.8 plots convergence of the objective function S after re-starting inversions from p207 with each plume removed and the original plume location “frozen” so that the plume is forbidden to return to its original location. The final $nRMS$ and roughness $R(m)$ for each case are plotted as points p301 and p302 on the trade-off diagram (Fig 3.3). P and $\delta\psi_\sigma$ test results at 1280 s are shown in Table 3.6.1: all four test criteria for significant change are met for each test. Removal of the DEEP moves the trade-off point further from p207 than removal of the SWAP, but in both cases $nRMS$ and $R(m)$ are substantially larger than for model p207. Thus the objective function is considerably larger. We conclude that both plumes are not artifacts and are required by our field data.

Slices and mapviews of models p301 and p302 (with p207 for comparison) are shown in Figure 3.9 and are quite interesting. We have dubbed the features around

the former DEEP and SWAP “halo-plumes” because in each case the inversion has constructed conductive paths around the excluded volume. Thus there is little doubt that the DEEP and SWAP exist. A remarkable coupling exists between the two halo-plumes. Removing the DEEP makes the SWAP more conductive and removing the SWAP makes the DEEP more conductive. We interpret this to mean that the model requires a specific amount of vertical current flow to fit the data: if the current can’t flow through one plume, it tries to increase current flow through the other plume to compensate.

Tests 2 (a – g) – Introduction of Gaps in the Plumes

The point of these tests is to systematically test the depth extent of the two plumes by examining the sensitivity of the data to the removal of segments of each plume. For the DEEP we remove segments: (a) from 100 to 347 km; (b) from 5 to 100 km; (c) from 5 to 32 km; (d) from 13 to 32 km; (e) from 5 to 13 km. For the SWAP we remove: (f) below 32 km and (g) from 7 to 32 km. The 1280 s period results are presented in Table 3.6.1. All four of the P and $\delta\sigma_\psi$ criteria for significant change are met for each test. Together these tests support the full depth extent of each feature.

Tests 3 (a – f): Vertical Current Blocking

When structure is 1D, MT source fields induce only horizontal current flow. Conductive plumes channel horizontally induced current into the vertical direction. To investigate how deep the current source must be, we can block the flow at successively deeper depths. Additionally we can investigate how far the plumes extend into the crust by blocking vertical current flow within the crust. Vertical current blocks were placed in the DEEP at (a) 347 km; (b) 199 km; (c) 100 km; (d) 32 km; and (e) 13 km. The only current block in the SWAP was placed at (f) 32 km. The results of these tests at 1280 s are summarized in Table 3.6.1. All four of the P and $\delta\sigma_\psi$ criteria for significant change are met for Tests 3b – 3f, but not for Test 3a. Test 3a may be

flawed because the surrounding mantle is conductive enough at this depth that the vertical current flow was not fully blocked by the resistive tablet. Together these tests support vertical current flow through the full depth extent of the DEEP and vertical current flow through the crust-mantle boundary of the SWAP.

3.7 Discussion

3.7.1 Comparison of SWAP & DEEP to regional geology

Figures 3.6(b – c) and 3.10 show that the SWAP has two conductive tendrils that approach the surface. One tendril is directly under the Caldera Payún Matrú. The other tendril is 100 km southwest of the Caldera Payún Matrú, directly under the Trómen Volcanic Field (TVF), which comprises the south-west portion of the PBP.

The TVF is similar to the rest of the PBP in age and composition. In particular, the TVF’s most recent volcanism has no arc signature and is interpreted to be from an intraplate source [*Ramos and Folguera, 2011*]. As no information about local volcanism was used in our inversions, the positioning of the SWAP tendrils is unlikely to be fortuitous.

The SWAP is east of both the expected mantle wedge location (visible in slice *C* of Figure 3.6(a)) and the main Andean volcanic arc. The SWAP remains above the subducted Nazca slab, with the most conductive part of the SWAP at ~ 50 km depth. Figs. 3.6(a) and 3.10 show that the SWAP dips west, apparently intersecting the subducted Nazca slab’s location at ~ 130 km depth. If the SWAP were connected to the slab, the recent volcanic products at the PBP could be expected to show an arc signature. However, since recent volcanism shows no arc signature, it is plausible that the SWAP does not connect to the subducted Nazca slab. In fact, while deeper portions of the DEEP were re-created in inversion p301 (section 3.6.1) and shown in Fig. 3.9 (p301), the deeper portion of the SWAP seems to have disappeared from inversion p302 (Fig. 3.9 (p302)). The SWAP is thus not required to extend to the

subducted Nazca slab's location at 130 km depth.

Fig. 3.11 shows that the SWAP coincides with the large subcrustal negative arrival identified by *Gilbert et al.* [2006] and *Wagner et al.* [2005] using receiver function analysis. *Gilbert et al.* [2006] suggest that this subcrustal negative is related to the back-arc volcanism. The SWAP's superposition with this negative arrival lends credence to our assertion that the SWAP is related to the root of the PBP volcanism.

Unlike the SWAP, Figures 3.6(a) and 3.10 show that the DEEP dips to the east, entering the top of the Mantle Transition Zone (MTZ) at roughly 400 km while remaining above the subducted Nazca slab. The DEEP can not be positively identified below 400 km, so it is not clear whether the DEEP rises from near the top of the MTZ or from a deeper source.

While the DEEP does not appear to “connect” to the Earth's surface directly under the Caldera Payún Matrú, it does approach the surface beneath the portion of the PBP known as the Auca Mahuida Volcanic Field (AMVF) 100 km southeast of the Caldera Payún Matrú (Fig. 3.10). The AMVF is geochemically and geochronologically similar to the rest of PBP, but with no volcanism younger than 0.8 Ma [*Ramos and Folguera*, 2011].

While the Payunia area shows obvious evidence of extension, a topographic profile along slice *C* (see Fig. 3.10) in Fig. 3.12 shows evidence of uplift and a significant change in topographic slope at the marked scarp. The footprint of the shallow portion of the DEEP correlates with this region of uplift and suggests that the DEEP has directly influenced this uplift.

While a fairly strong resistor (>1000 Ohm-m) separates the DEEP and SWAP by at least 100 km at most depths (see Fig. 3.6(a)), it is possible that the DEEP and SWAP are connected shallowly above ~ 7 km. In fact, slice *a* of Fig. 3.9 (p207), taken at ~ 5 km, shows conductivity beneath the PBP that spans the location of DEEP and SWAP. Shallower than ~ 5 km (DEEP) and ~ 7 km (SWAP), the model was generally more conductive, and it was not possible to positively identify either

Table 3.1: Hypothesis test results at 1280 s. A total of 37 sites were used at this period for both the P -tests and the $\delta\psi_\sigma$ -tests: columns other than Global $nRMS$ indicate the number of sites in each category. See text for discussion of each test. Global $nRMS$ represents $nRMS$ at all sites and periods used in the inversion. For comparison, global $nRMS$ for p207 is 1.560.

Test No.	Global $nRMS$	$1 < P < 2$	$P > 2$	$1 < \delta\psi_\sigma < 2$	$\delta\psi_\sigma > 2$	Test Description
1a	4.812	1	36	5	28	removal of DEEP from 4.6 km – 347 km
1b	3.486	10	27	9	18	removal of SWAP from 6.8 km – 199 km
2a	2.455	12	25	4	28	removal of DEEP from 103 km – 347 km
2b	4.319	8	29	7	25	removal of DEEP from 4.6 km – 103 km
2c	3.290	15	19	12	11	removal of DEEP from 4.6 km – 32.6 km
2d	2.006	22	10	8	8	removal of DEEP from 12.9 km – 32.6 km
2e	2.382	21	10	8	4	removal of DEEP from 4.6 km – 12.9 km
2f	3.214	12	25	10	15	removal of SWAP from 32.6 km – 199 km
2g	1.991	30	5	6	5	removal of SWAP from 6.8 km – 32.6 km
3a	1.579	22	0	2	0	vertical current block of DEEP at 347 km
3b	1.966	27	8	6	25	vertical current block of DEEP at 199 km
3c	2.545	16	21	6	27	vertical current block of DEEP at 103 km
3d	2.670	15	20	7	18	vertical current block of DEEP at 32.6 km
3e	2.431	16	17	9	10	vertical current block of DEEP at 12.9 km
3f	2.490	23	14	8	10	vertical current block of SWAP at 32.6 km
301	2.001	31	4	5	14	converged inv., model “frozen” at Test 1a DEEP location
302	1.900	31	5	8	15	converged inv., model “frozen” at Test 1b SWAP location

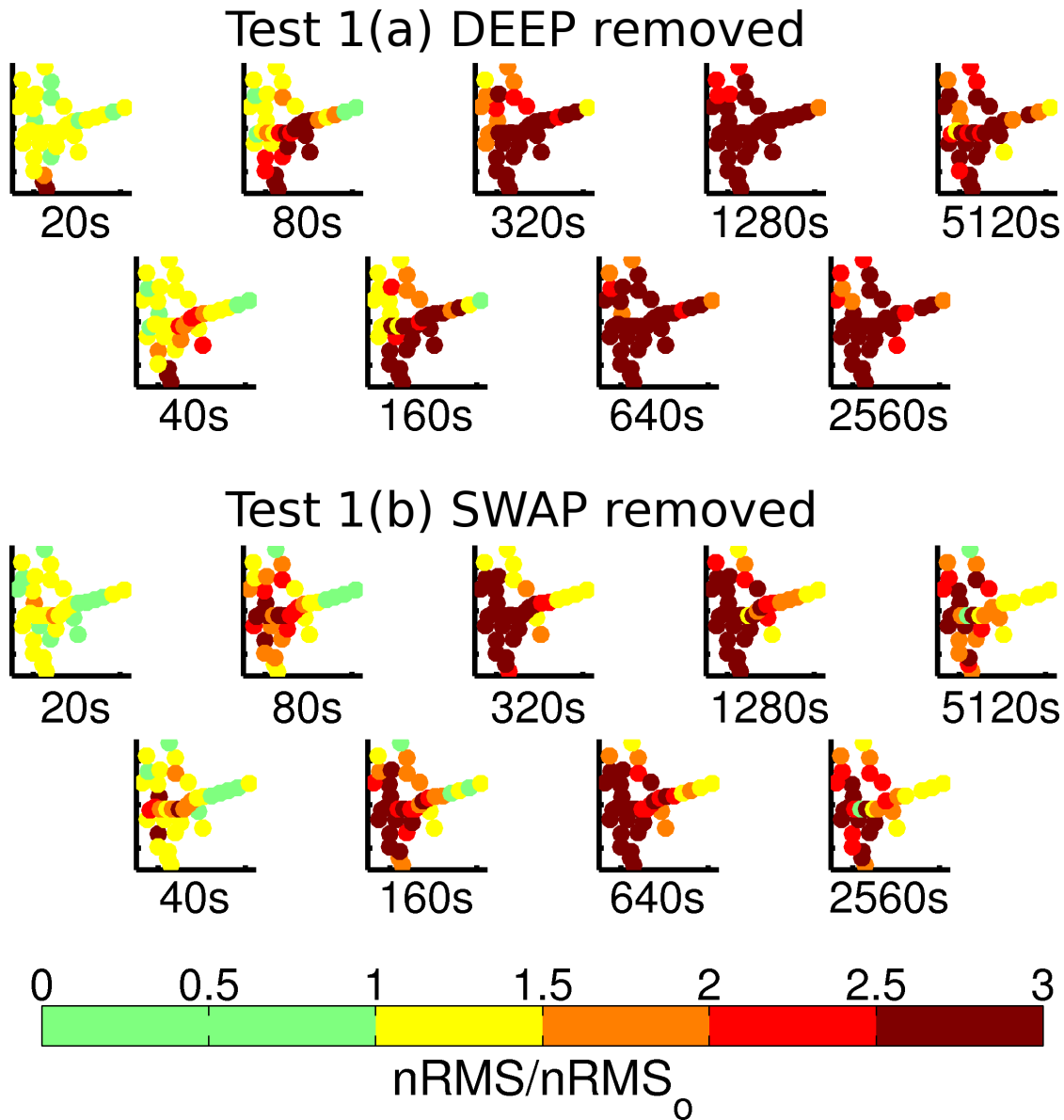


Figure 3.6: Map views showing $P = nRMS/nRMS_0$ at each site at each period with the DEEP removed (Test 1(a) as discussed in the text) and SWAP removed (Test 1(b)). Green values are considered insignificant change from the original model. Note that the effect of removing either plume is larger at longer periods.

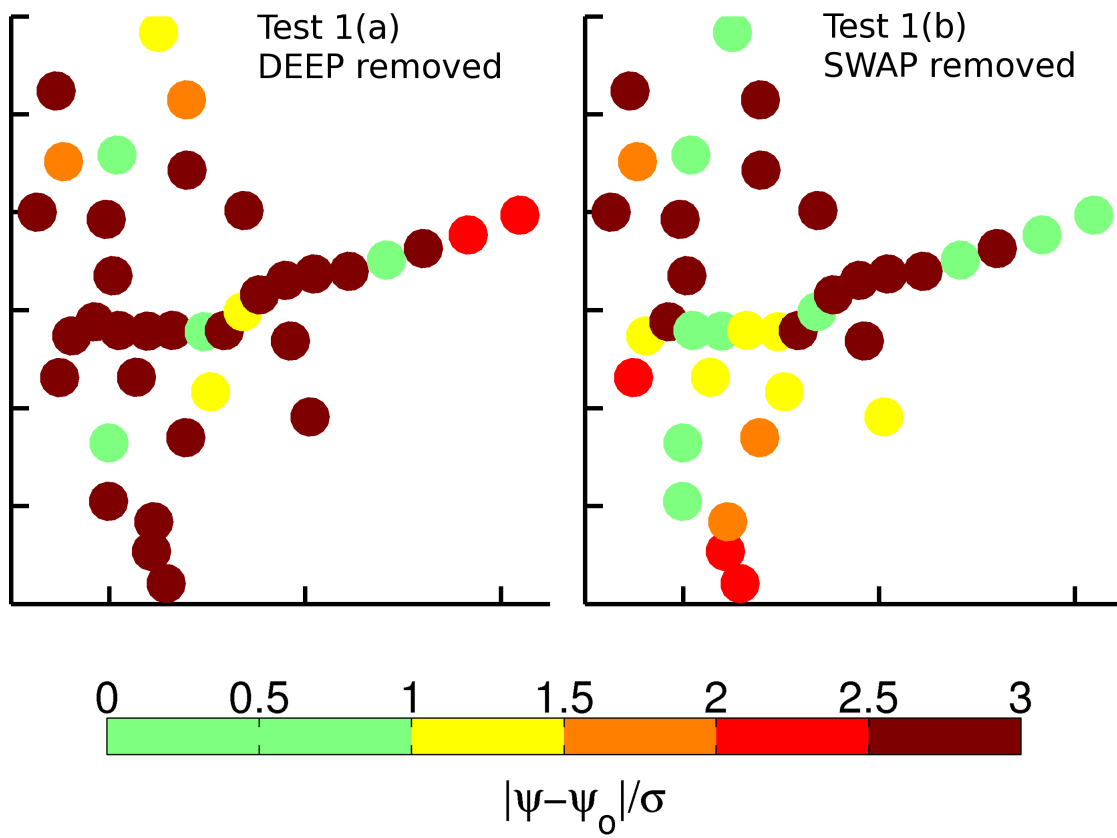


Figure 3.7: Map views showing $\delta\psi_\sigma$ at each site at 1280 s with the DEEP removed (Test 1(a) as discussed in the text) and SWAP removed (Test 1(b)). Green values are considered insignificant change from the original model.

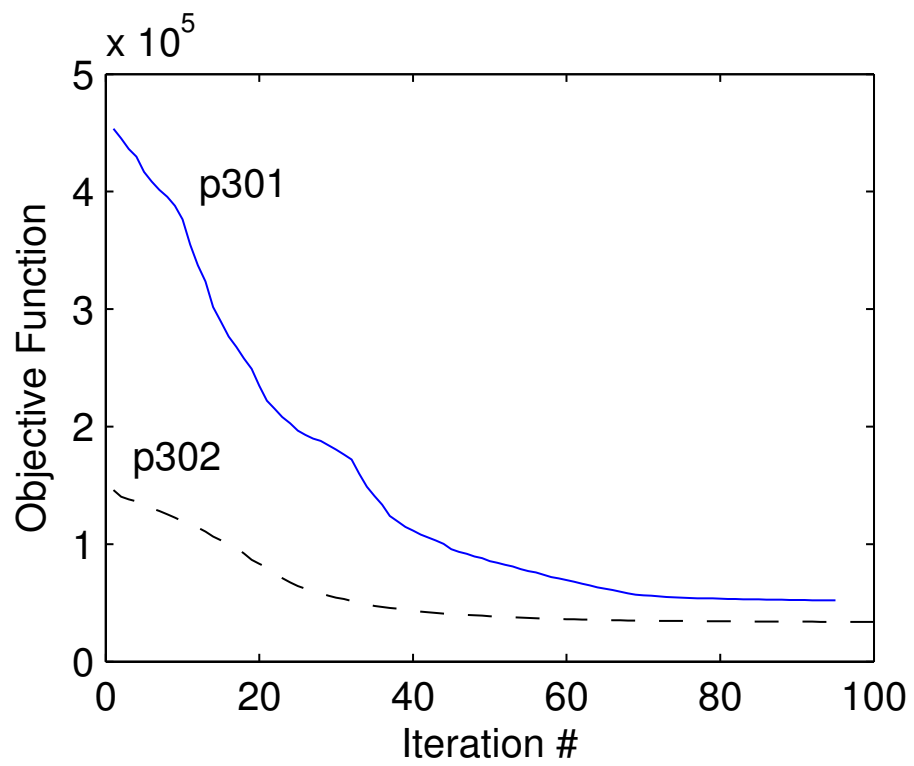


Figure 3.8: A plot of objective function versus number of iterations for p301 and p302 shows that each inversion's objective function has converged.

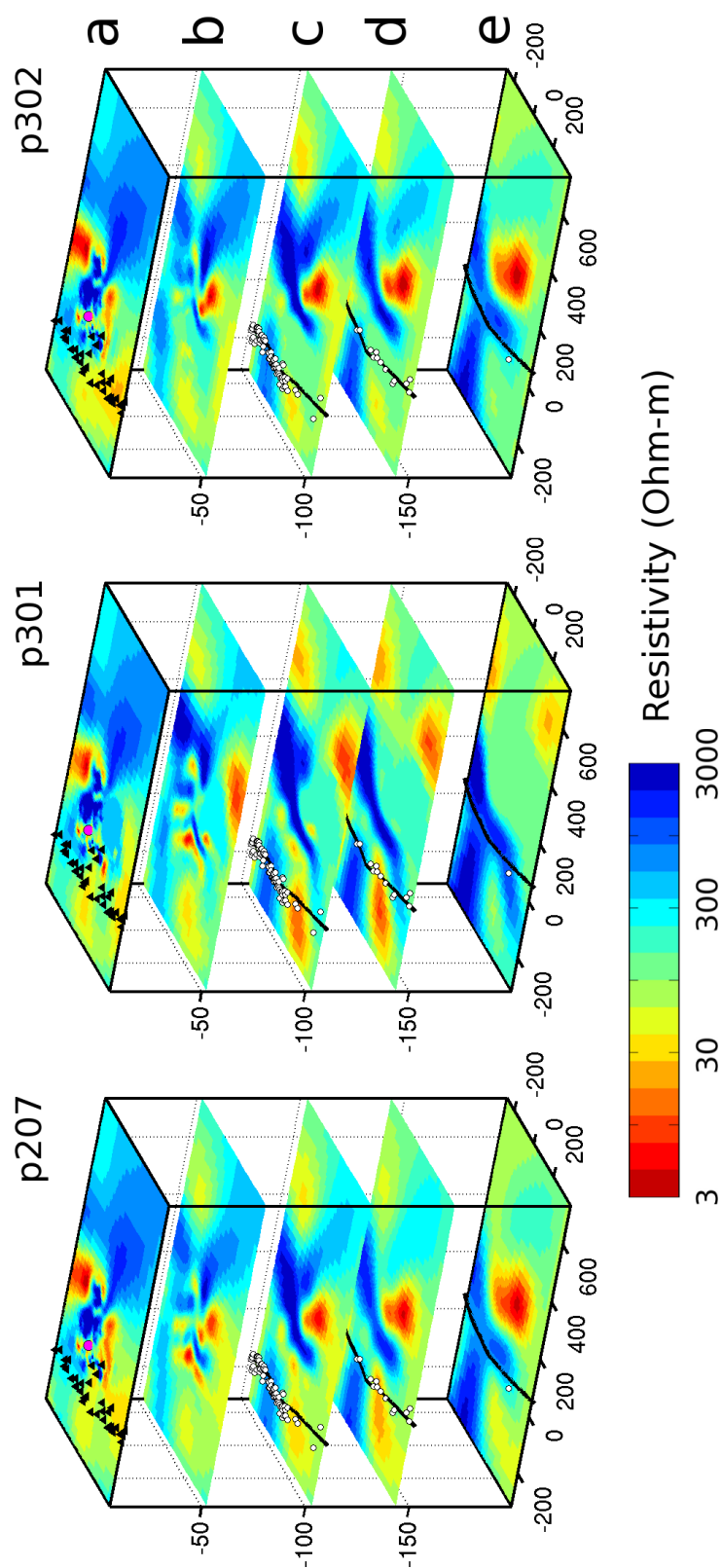


Figure 3.9: Map legend same as Fig. 3.6(a), but images are map-view slices of resistivity through models p207, p301, and p302 at different depths. Map-views’ “east-west” direction is parallel to slices $A - E$ shown on Fig. 3.1(b), with each horizontal slice taking up roughly the area spanned by the five original east-west slices.

DEEP or SWAP for additional model assessment. This electrically conductive shallow connection almost certainly stems from increased water within the Neuquén basin sedimentary rock that underlies much of the PBP. There is a single young monogenetic volcanic center between the TVF and Auca Mahuida Volcanic Field (see Fig. 3.10), but no other evidence of < 2 Ma volcanism between the TVF and the Auca Mahuida Volcanic Field. Given additional evidence against a PBP near-surface basaltic reservoir [Hernando *et al.*, 2012; Folguera *et al.*, 2009], the shallow electrical connection between DEEP and SWAP is unlikely to represent partial melt.

3.7.2 Comparison to other electrical conductivity models

A structure closely resembling the DEEP was previously identified by Burd *et al.* [2008] as a result of a 2D MT inversion using a subset of the 37 sites included in this paper’s work. This result (shown in Ramos and Folguera [2011]) was interpreted to indicate current flow between MTZ and the shallow crust. It appeared to surface under the PMVF, which suggested a deep source for the PMVF volcanism. However, Figure 3.10 shows that the DEEP surfaces over 100 km to the south-east, at the Auca Mahuida Volcanic Field. This earlier 2D work was likely negatively affected by the attempt to fit 3D data with a 2D model.

The DEEP has strong similarities to, but significant differences from, a deep conductive plume studied by Burd *et al.* [2013]. This deep “flatslab” plume is 600 km north of the DEEP and just east of the region of Pampean Shallow Subduction. The flatslab plume is capped at 100 km depth where Burd *et al.* [2013] suggest it cannot penetrate compressive lithosphere, while the DEEP appears to rise into the crust.

An additional important difference is that the flatslab plume penetrates the down-dip extrapolation of the flatslab while the DEEP remains parallel to the projected subducted Nazca slab as depth increases. Burd *et al.* [2013] invoke a slab window to explain the flatslab plume’s interaction with the slab. However, while there is no need for a slab window above 400 km at the DEEP location, the slab and the DEEP

would intersect in the MTZ. There are two possible scenarios. First, the slab does not extend below 400 km (and there is no evidence that it does) and does not exist south of the tear suggested by *Pesicek et al.* [2012] (shown in Fig. 3.10). In this case, the DEEP could continue through the MTZ into the DEEP mantle. In the second scenario, the slab below 400 km is responsible for generating the DEEP, perhaps by local introduction of water into the MTZ.

Newberry Volcano in Oregon, USA, in the back-arc of the Cascades appears to be arguably similar to the PMVF and PBP. *Egbert et al.* [2012] identify an arguably 500 km deep electrically conductive plume similar to our DEEP rising vertically beneath Newberry. Newberry and the Cascadia Subduction Zone have been studied extensively, with *Long et al.* [2012] proposing that the Miocene shallow slab steepening and trench roll-back drive westward mantle corner flow, subsequent upper plate extension and back-arc volcanic upwelling.

3.7.3 DEEP & SWAP: indicators of mantle flow

Our SWAP and DEEP are compatible with an interpretation related to *Long et al.* [2012]’s Cascadia discussion applied to the Andean back-arc. As the subducted slab steepens, the mantle must flow into the region between the slab and the lithosphere. The largely intraplate signature of the < 2 Ma PBP volcanism is compatible with this mantle flow [*Germa et al.*, 2010; *Kay et al.*, 2006]. *Gilbert et al.* [2006] also propose that mantle corner flow may play a role in the back-arc volcanism of this region. If there is also a slab tear south of 38° S as suggested by *Pesicek et al.* [2012], this flow would be towards the north-west rather than due west, as material wells up around the southern edge of the Nazca slab.

We propose that this northwesterly flow has decapitated the DEEP to form the SWAP. During the Miocene shallow subduction regime, the SWAP was a part of the DEEP (Fig. 3.7.3(a)). However, as trench roll-back and slab deepening began to occur at the beginning of the Pliocene, the SWAP was sheared off and pulled to the

north-west (away from the DEEP) as mantle flowed into the area formerly occupied by the Nazca slab (Fig. 3.7.3(b)). The contours and slab location in Fig. 3.7.3(c) are not a cartoon – they are from slice C of Fig. 3.6(a) as shown on Fig 3.12. In this interpretation, the depth of greatest horizontal displacement of the SWAP from the DEEP represents the depth of greatest upper mantle flow velocity. Thus the SWAP tilts downward to the north-west and the DEEP tilts upward to the north-west, indicating greatest flow velocity near 130 km depth. Given additional time, as trench rollback & slab deepening continue and the DEEP continues to rise to the surface, the DEEP will continue to be caught in the mantle shear to the north-west and may undergo additional decapitation. If this process continues, we might expect renewed volcanism at Auca Mahuida.

The mantle flow velocity under South America since the Pliocene has the same order of magnitude as South America’s velocity relative to the deep mantle. South America is moving 45 km/Ma in a hot-spot reference frame, so over 5 Ma (since the beginning of the Pliocene) the SWAP has likely moved ~ 225 km. SWAP and DEEP are separated by ~ 200 km at 130 km depth, which is compatible with our estimation of SWAP movement.

In our mantle-flow interpretation, the PBP should have been more active in the past when extension associated with the trench roll-back and slab deepening first allowed eruption of the pond of SWAP magma that had formed at the base of the compressional crust during the Miocene shallow subduction regime. Some volcanism associated with the SWAP continues to occur, but the magma flux is much less than it was 1.7 Ma ago [*Germa et al.*, 2010; *Ramos and Folguera*, 2011].

3.8 Conclusion

3D minimum-structure inversions of magnetotelluric data yield an image of the electrical conductivity beneath the Payún Matrú Volcanic Field in western Argentina. We have demonstrated the existence of an electrically conductive plume (the DEEP)

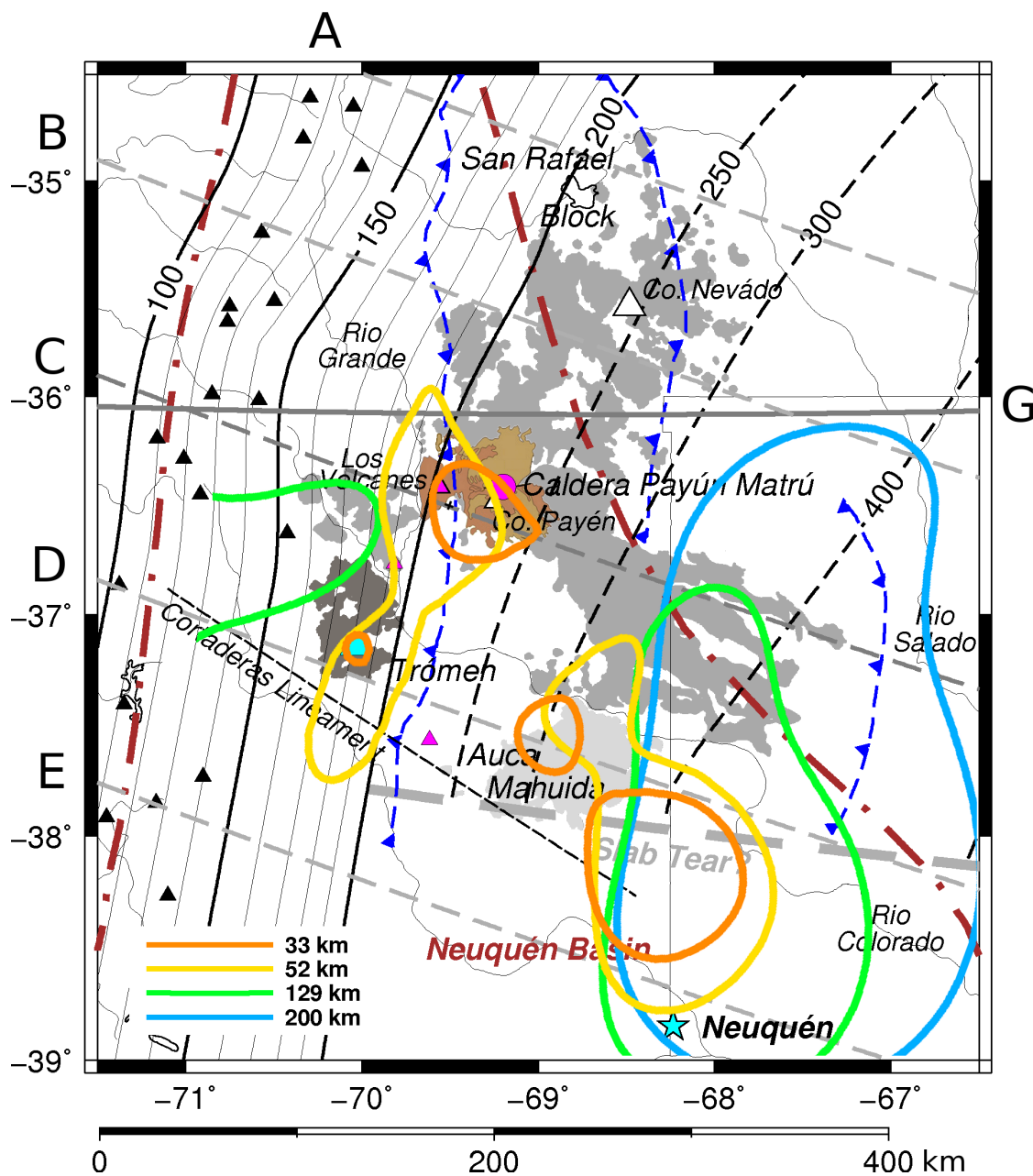


Figure 3.10: Figure is identical to Fig. 3.1(a), with addition of contours corresponding to 35 Ohm-m isosurface of DEEP and SWAP at 33, 52, 129, and 200 km. Transect *G* shows position of seismic receiver function work of *Gilbert et al.* [2006] discussed in connection with Fig. 3.11.

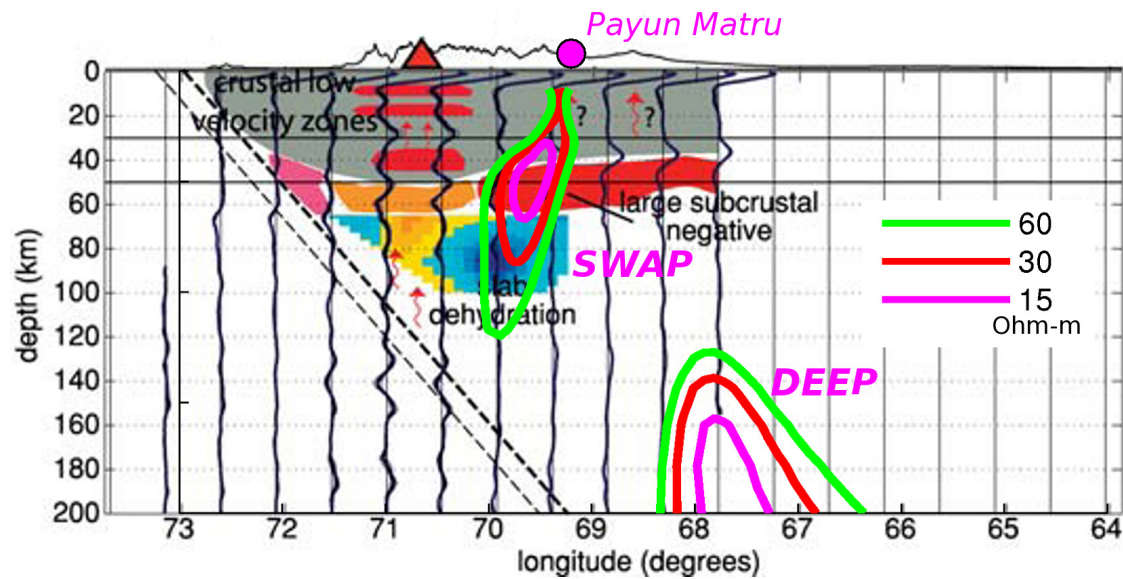


Figure 3.11: 60, 30, and 15 Ohm-m contours for SWAP and DEEP from slice *C* of Figs. 3.1(b) and 3.6(a), superimposed on a receiver function-derived diagram from *Gilbert et al.* [2006] that corresponds to transect G on Fig. 3.10.

that extends from 5 km below Payunia (and possibly shallower) to at least 347 km depth, dipping to the east and remaining above the subducted Nazca slab. We have also demonstrated the existence of an electrically conductive plume (the SWAP) that extends from 7 km (and possibly shallower) below the Caldera Payún Matrú and the Trómen Volcanic Field to roughly 130 km depth, dipping to the west and remaining above the subducted Nazca slab. While the DEEP has relatively constant conductivity at all depths, the SWAP is most conductive near 50 km depth.

The DEEP and SWAP conductivity and the PBP volcanism are best explained by a partially melted mantle plume. This plume has been sheared by the north-westward shallow mantle corner flow to form the previously connected SWAP and DEEP.

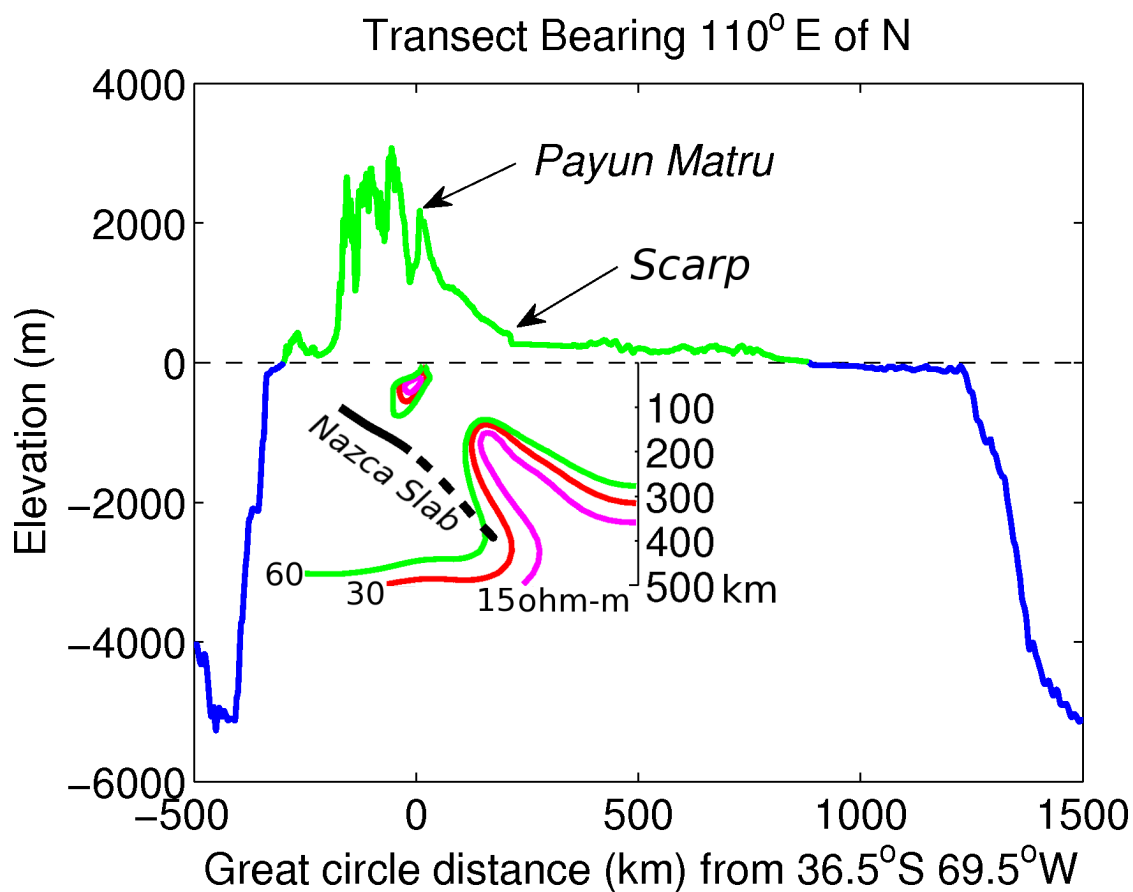
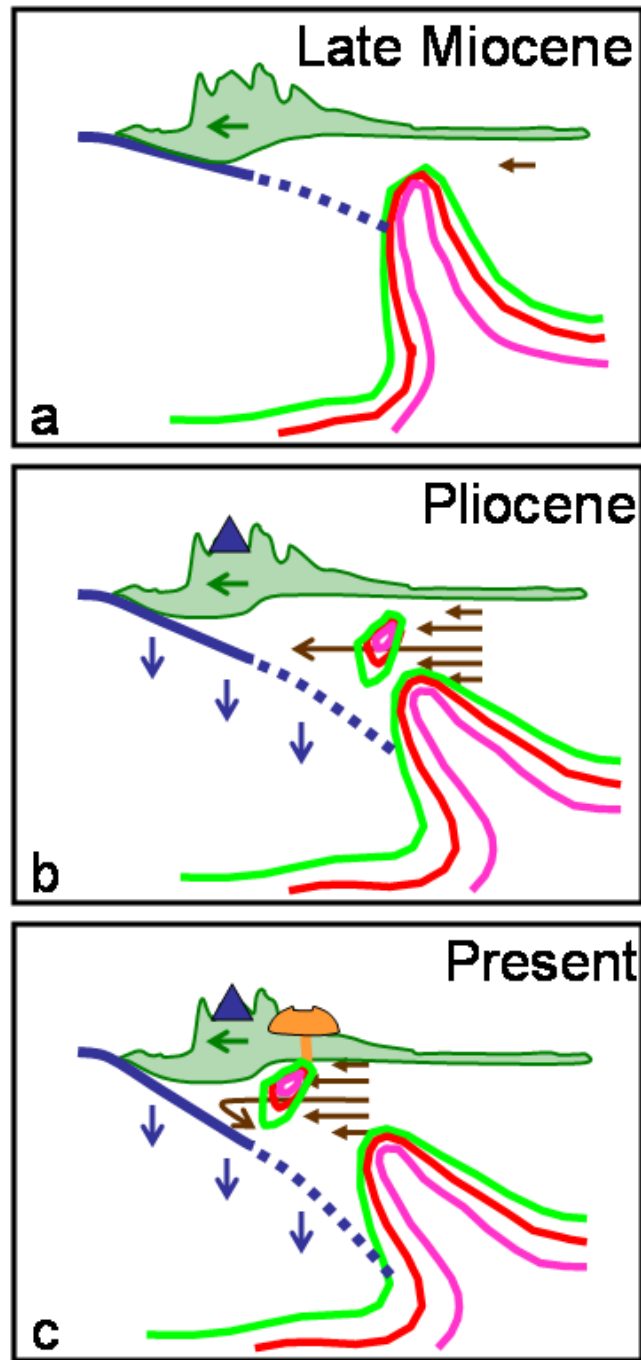


Figure 3.12: Topographic transect along slice C of Figs. 3.6(a) and 3.10 shows depth of both Pacific and Atlantic Oceans. Inset shows SWAP, DEEP, and subducted Nazca slab, also from slice C: shallowest portion of DEEP corresponds to marked scarp, while SWAP corresponds to Payún Matru.

Figure 3.13: Three cartoons depicting evolution of present-day PBP, SWAP, and DEEP. 60, 30, & 15 Ohm-m contours of SWAP & DEEP in green, red, & magenta; subducted Nazca slab location in solid or dashed blue line; Nazca slab motion vectors in blue; mantle flow vectors in brown; PBP in tan; active SVZ at dark blue triangle. (a) shows situation during the end of the Miocene shallow subduction regime, when DEEP and SWAP were one structure just beginning to be sheared north-westward; (b) slab steepening continues through Pliocene, causing increase in mantle flow which shears SWAP and DEEP to north-west, eventually decapitating DEEP to form SWAP; (c) present-day situation based on slice C of Fig. 3.6 – SWAP, DEEP, Nazca slab are to scale, with South America, SVZ, and PBP at correct locations but with exaggerated height.



3.9 Data Availability

The MT data used in this paper are available through the *IRIS Data Management System, Seattle, Washington*.

3.10 Acknowledgments

This project is supported by the U.S. National Science Foundation (NSF) Grants EAR9909390, EAR0310113 and EAR0739116 and U.S. Department of Energy Office of Basic Energy Sciences grant DE-FG03-99ER14976. MT equipment is from the EMSOC Facility supported by NSF Grants EAR9616421 and EAR0236538. This project also received support from the Agencia Nacional de Promoción Científica y Tecnológica PICT 2005 No. 38253. The first author received support from the Seattle Chapter of the ARCS Foundation, and from Graduate Research Support, Qamar, Stephens, and Coombs Fellowships provided by the Dept. of Earth and Space Sciences, University of Washington. Thank you to Jimmy Larsen for numerous helpful discussions. Gabriel Giordanengo of Instituto de Geocronología y Geología Isotópica provided extensive assistance in the field.

BIBLIOGRAPHY

- Anderson, M., P. Alvarado, G. Zandt, and S. Beck, Geometry and brittle deformation of the subducting Nazca Plate, Central Chile and Argentina, *Geophysical Journal International*, 171, 419–434, doi:10.1111/j.1365-246X.2007.03483.x, 2007.
- Bahr, K., Interpretation of the magnetotelluric impedance tensor regional induction and local telluric distortion, *Journal of Geophysics*, 62(2), 119–127, 1988.
- Bercovici, D., and S. Karato, Whole mantle convection and the transition-zone water filter, *Nature*, 425, 39–44, doi:10.1038/nature01918, 2003.
- Bermúdez, A., D. Delpino, F. Frey, and A. Saal, Los basaltos de retroarco extrandinos, *Geologia*, pp. 161–172, ramos, V. ed. Geologia y recursos naturales de Mendoza, Relatorio, XII Congreso Geológico Argentino y II Congreso Exploración de Hidrocarburos, Assoc. Geol Argentina y Inst, Argentino del Petróleo, 1993.
- Booker, J. R., The Magnetotelluric Phase Tensor: A Critical Review, *Surveys in Geophysics*, doi:10.1007/s10712-013-9234-2, 2013.
- Booker, J. R., A. Favetto, and M. C. Pomposiello, Low Electrical Resistivity associated with plunging of the Nazca flat slab beneath Argentina, *Nature*, 429, 399–403, doi:10.1038/nature02565, 2004.
- Booker, J. R., A. Favetto, M. C. Pomposiello, and F. Xuan, The roll of fluids in the Nazca flat slab near 31s revealed by the electrical resistivity structure, in *6th International Symposium on Andean Geodynamics, Barcelona, Spain, Extended Abstracts*, pp. 119–122, IRD Editions, 2005, ISBN: 2-7099-1575-8, 2005.

- Burd, A. I., J. R. Booker, M. C. Pomposiello, A. Favetto, J. Larsent, G. Giordanengo, and L. Orozco Bernal, Electrical conductivity beneath the Payún matrú volcanic field in the andean back-arc of argentina near 36.5° S: insights into the magma source, in *7th. International Symposium on Andean Geodynamics, Nice, France, Extended Abstracts*, pp. 90–93, 2008.
- Burd, A. I., J. R. Booker, R. L. Mackie, M. C. Pomposiello, and A. Favetto, Electrical conductivity of the Pampean Shallow Subduction Region of Argentina near 33° S: evidence for a slab window, *Geochemistry Geophysics Geosystems*, in press, MS No. 2013GC004732, 2013.
- Cahill, T., and B. Isacks, Seismicity and Shape of the Subducted Nazca Plate, *Journal of Geophysical Research*, *97*, 17,503–17,529, doi:10.1029/92JB00493, 1992.
- Caldwell, G. C., H. M. Bibby, and C. Brown, The Magnetotelluric Phase Tensor, *Geophysical Journal International*, *158*, 457–469, doi:10.1111/j.1365-246X.2004.02281.x, 2004.
- Chen, P.-F., C. R. Bina, and E. A. Okal, Variations in slab dip along the subducting Nazca Plate, as related to stress patterns and moment release of intermediate-depth seismicity and to surface volcanism, *Geochemistry Geophysics Geosystems*, *2*, doi:10.1029/2001GC000153, 2001.
- Creager, K. C., L. Chiao, J. P. Winchester, and E. R. Engdahl, Membrane Strain Rates in the Subducting Plate Beneath South America, *Geophysical Research Letters*, *22*(16), 2321–2324, doi:10.1029/95GL02321, 1995.
- Egbert, G., Robust multiple-station magnetotelluric data processing, *Geophysical Journal International*, *130*, 475–496, doi:10.1111/j.1365-246X.1997.tb05663.x, 1997.

- Egbert, G. D., N. Meqbel, P. Wannamaker, A. Schultz, and A. Kelbert, Three-dimensional Inversion of EarthScope Magnetotelluric Data: crustal and mantle conductivity beneath the NW USA, IRIS Webinar, 2012.
- Folguera, A., and V. Ramos, Collision of the Mocha fracture zone and a <4 Ma old wave of orogenic uplift in the Andes (36 – 38 S), *Lithosphere*, 1, 364–369, doi: 10.1130/L66.1, 2009.
- Folguera, A., T. Zapata, and V. Ramos, Late Cenozoic extension and the evolution of the Neuquen Andes, in *Evolution of the Andean Margin: A tectonic and magmatic view from the Andes to the Neuquen Basin (35- 39S lat)*, vol. 407, edited by S. Kay and V. Ramos, pp. 267–286, Geological Society of America, 2006.
- Folguera, A., J. A. Naranjo, Y. Orihashi, H. Sumino, K. Nagao, E. Polanco, and V. A. Ramos, Retroarc volcanism in the northern san rafael block (34° – 35° 30' s), southern Central Andes: Occurrence, age, and tectonic setting, *Journal of Volcanology and Geothermal Research*, 186, 169–185, doi:10.1010/j.jvolgeores.2009.06.012, 2009.
- Gans, C. R., S. L. Beck, G. Zandt, H. Gilbert, P. Alvarado, M. Anderson, and L. Linkimer, Continental and oceanic crustal structure of the Pampean flat slab region, western Argentina, using receiver function analysis: new high-resolution results, *Geophysical Journal International*, 186, 45–58, doi: 10.1111/j.1365-246X.2011.05023.x, 2011.
- Germa, A., X. Quidelleur, P. Y. Gillot, and P. Tchilinguirian, Volcanic evolution of the back-arc Pleistocene Payun Matru volcanic field, Argentina, *Journal of South American Earth Sciences*, 29, 717–730, doi:10.1016/j.jsames.2010.01.002, 2010.
- Gilbert, H., S. Beck, and G. Zandt, Lithospheric and upper mantle structure of central Chile and Argentina, *Geophysical Journal International*, 165, 383–398, doi: 10.1111/j.1365-246X.2006.02867x, 2006.

- Groom, R. W., and R. C. Bailey, Decomposition of magnetotelluric impedance tensors in the presence of local three dimensional galvanic distortion, *Journal of Geophysical Research*, *94*, 1913–1925, doi:10.1029/JB094iB02p01913, 1989.
- Hernando, I. R., E. J. Llambías, P. D. González, and K. Sato, Volcanic stratigraphy and evidence of magma mixing in the quaternary Payún Matrú volcano, Andean backarc in western Argentina, *Andean Geology*, *39*, 158–179, 2012.
- Howell, J. A., E. Schwarz, L. A. Spalletti, and G. D. Veiga, The Neuquén Basin: an overview, in *The Neuquén Basin, Argentina: A Case Study in Sequence Stratigraphy and Basin Dynamics*, vol. 252, pp. 1–14, Geological Society, London, doi: 10.1144/GSL.SP.2005.252.01.01, 2005.
- <http://www.globalcmt.org/CMTsearch.html>, Global Centroid Moment Tensor solutions.
- Inbar, M., and C. Risso, Holocene Yardangs in Volcanic Terrains in the Southern Andes, Argentina, *Earth Surface Processes and Landforms*, *26*, 657–666, doi: 10.1002/esp.207, 2001a.
- Inbar, M., and C. Risso, A morphological and morphometric analysis of a high density cinder cone volcanic field – Payun Matru, south-central Andes, Argentina, *Zeitschrift fur Geomorphologie*, *45*(3), 321–343, 2001b.
- International Seismological Centre, EHB Bulletin, <http://www.isc.ac.uk>, Internatl. Seis. Cent., Thatcham, United Kingdom, 2010.
- IRIS Data Management System, Seattle, Washington, the facilities of the IRIS Data Management System, and specifically the IRIS Data Management Center, were used for access to waveform, metadata or products required in this study. The IRIS DMS is funded through the National Science Foundation and specifically the GEO Directorate through the Instrumentation and Facilities Program of the National

Science Foundation under Cooperative Agreement EAR-0552316. Some activities of are supported by the National Science Foundation EarthScope Program under Cooperative Agreement EAR-0733069.

Jones, A. G., Distortion of magnetotelluric data: its identification and removal, in *The Magnetotelluric Method Theory and Practice*, edited by A. Chave and A. Jones, Cambridge University Press, doi:10.1017/CBO9781139020138.008, 2012.

Kay, S. M., W. Burns, P. Copeland, and O. Mancilla, Upper Cretaceous to Holocene magmatism and evidence for transient Miocene shallowing of the Andean subduction zone under the northern Neuquen Basin, in *Evolution of the Andean Margin: A tectonic and magmatic view from the Andes to the Neuquen Basin (35- 39S lat)*, vol. 407, edited by S. Kay and V. Ramos, pp. 19–60, Geological Society of America, 2006.

Li, C., R. D. van der Hilst, E. R. Engdahl, and S. Burdick, A new global model for P wave speed variations in Earth's mantle, *Geochemistry Geophysics Geosystems*, 9(5), Q05,018, doi:10.1029/2007GC001806, 2008.

Linkimer Abarca, L., Lithospheric Structure of the Pampean Flat Slab (Latitude 30-33S) and Northern Costa Rica (Latitude 9-11N) Subduction Zones, Ph.D. thesis, University of Arizona, Tucson, Arizona, 2011.

Long, M. D., et al., Mantle dynamics beneath the Pacific Northwest and the generation of voluminous back-arc volcanism, *Geochemistry Geophysics Geosystems*, 13(1), doi:10.1029/2012GC004189, 2012.

Mackie, R. L., and M. Watts, Detectability of 3-D sulphide targets with AFMAG, *SEG Technical Program Expanded Abstracts*, pp. 1–4, doi:10.1190/segam2012-1248.1, 2012.

- Mackie, R. L., W. Rodi, and M. D. Watts, 3-D magnetotelluric inversion for resource exploration, in *SEG 2001 Technical Program Expanded, San Antonio, Texas*, 2001.
- Pardo, M., D. Comte, and T. Monfret, Seismotectonic and stress distribution in the central Chile subduction zone, *Journal of South American Earth Sciences*, *15*, 11–22, doi:10.1016/S0895-9811(02)00003-2, 2002.
- Pesicek, J. D., E. R. Engdahl, C. H. Thurber, H. R. DeShon, and D. Lange, Mantle subducting slab structure in the region of the 2010 M8.8 Maule earthquake (30–40 S), Chile, *Geophysical Journal International*, *191*, 317–324, doi:10.1111/j.1365-246X.2012.05624.x, 2012.
- Petiau, G., Second Generation of Lead-lead Chloride Electrodes for Geophysical Applications, *Pure and Applied Geophysics*, *157*(3), 357–382, doi:10.1007/s000240050004, 2000.
- Poe, B. T., C. Romano, F. Nestola, and J. R. Smyth, Electrical conductivity anisotropy of dry and hydrous olivine at 8 GPa, *Physics of the Earth and Planetary Interiors*, *181*, 103 – 111, doi:10.1016/j.pepi.2010.05.003, 2010.
- Ramos, V. A., Los depósitos sinorogénicos terciarios de la región Andina, in *Geología Argentina*, vol. 29, edited by R. Caminos, pp. 651–682, Servicio Geológico Minero Argentino (SEGEMAR), 1999.
- Ramos, V. A., Anatomy and global context of the Andes: Main geologic features and the Andean orogenic cycle, in *Backbone of the Americas: Shallow Subduction, Plateau Uplift, and Ridge and Terrane Collision*, vol. 204, edited by S. Kay, V. Ramos, and W. Dickinson, pp. 31–65, Geological Society of America, doi:10.1130/2009.1204(02), 2009.
- Ramos, V. A., The Grenville-age basement of the Andes, *Journal of South American Earth Sciences*, *29*, 77–91, doi:10.1016/j.jsames.2009.09.004, 2010.

- Ramos, V. A., and A. Folguera, Payenia volcanic province in the Southern Andes: An appraisal of an exceptional Quaternary tectonic setting, *Journal of Volcanology and Geothermal Research*, 201, 53–64, doi:10.1016/j.jvolgeores.2010.09.008, 2011.
- Ramos, V. A., and S. M. Kay, Overview of the tectonic evolution of the southern Central Andes of Mendoza and Neuquen (35–39s latitude), in *Evolution of the Andean Margin: A tectonic and magmatic view from the Andes to the Neuquen Basin (35–39S lat)*, vol. 407, edited by S. Kay and V. Ramos, pp. 1–17, Geological Society of America, 2006.
- Rodi, W., and R. L. Mackie, Nonlinear Conjugate Gradients Algorithm for 2-D Magnetotelluric Inversion, *Geophysics*, 66, 174–187, doi:10.1190/1.1444893, 2001.
- Rodi, W. L., and R. L. Mackie, The inverse problem, in *The Magnetotelluric Method Theory and Practice*, edited by A. D. Chave and A. G. Jones, pp. 347–420, Cambridge University Press, 2012.
- Schilling, F. R., G. Partzsch, H. Brasse, and G. Schwarz, Partial melting below the magmatic arc in the central Andes deduced from geoelectromagnetic field experiments and laboratory data, *Physics of the Earth and Planetary Interiors*, 103, 17–31, doi:10.1016/S0031-9201(97)00011-3, 1997.
- Slancová, A., A. Špičák, V. Hanuš, and J. Vaněk, Delimitation of domains with uniform stress in the subducted Nazca plate, *Tectonophysics*, 319, 339–364, doi:10.1016/S0040-1951(99)00302-9, 2000.
- Smith, J. T., and J. R. Booker, Rapid inversion of two- and three-dimensional magnetotelluric data, *Journal of Geophysical Research*, 96, 3905–3922, doi:10.1029/90JB02416, 1991.
- Tebbens, S. F., and S. C. Cande, Southeast Pacific tectonic evolution from early

- Oligocene to Present, *Journal of Geophysical Research*, *102*, 12,061–12,084, doi:10.1029/96JB02582, 1997.
- Wagner, L. S., S. L. Beck, and G. Z. F. ME, Upper mantle structure in the south central Chilean subduction zone (30 to 36S), *Journal of Geophysical Research*, *110*(B1), doi:10.1029/2004JB003238, 2005.
- Xu, Y., T. Brent, T. Poe, T. Shankland, and D. Rubie, Electrical conductivity of olivine, wadsleyite and ringwoodite under upper-mantle conditions, *Science*, *280*, 1415–1418, doi:10.1126/science.280.5368.1415, 1998.
- Xu, Y., T. Shankland, and T. Poe, Laboratory-based electrical conductivity in the earth's mantle, *Journal of Geophysical Research - Solid Earth*, *105*(B12), 27,865–27,875, doi:10.1029/2000JB900299, 2000.
- Yoshino, T., Laboratory Electrical Conductivity Measurement of Mantle Minerals, *Surveys in Geophysics*, *31*, 163–206, doi:10.1007/s10712-009-9084-0, 2010.
- Yoshino, T., T. Matsuzaki, A. Shatskiy, and T. Katsura, The effect of water on the electrical conductivity of olivine aggregates and its implications for the electrical structure of the upper mantle, *Earth and Planetary Science Letters*, *2008*, 291–300, doi:10.1016/j.epsl.2009.09.032, 2009.
- Yoshino, T., A. Shimojuku, S. Shan, X. Guo, D. Yamazaki, E. Ito, Y. Higo, and K. Funakoshi, Effect of temperature, pressure and iron content on the electrical conductivity of olivine and its high-pressure polymorphs, *Journal of Geophysical Research*, *117*, doi:10.1029/2011JB008774, 2012.

VITA

Education

- B.S. in Physics, Harvey Mudd College, 2005.
- M.S. in Earth and Space Sciences, University of Washington, 2009.

Selected awards and honors

- UW ESS Department Coombs Excellence in Teaching Award, 2012.
- UW ESS Department Awards (including Tony Qamar Award and Dorothy G. Stephens Fellowship): 2007, 2010, 2011.
- ARCS Foundation Scholar, Seattle Chapter, 2005 – 2007.
- All-Ireland Silver Medalist, Senior Fiddle Slow Airs, at Fleadh Cheoil na hEireann (Ireland's national traditional music festival and competition), 2009.

Aurora Burd currently lives in the Seattle area.

She can be contacted at Aurora_Burd@alumni.hmc.edu.